Investigating the Modification of Spontaneous Emission using Layer-by-Layer Self-Assembly

Islam Ahmed Ibrahim Youssef Ashry

Dissertation submitted to the faculty of the
Virginia Polytechnic Institute and States University
In partial fulfillment of the requirements for the degree of

Doctor of Philosophy

in

Electrical Engineering

Yong Xu, Chair

Ali Mohamed Okaz

Anbo Wang

Gray R. Pickrell

Sedki Mohamed Riad

James Randy Heflin

December 3, 2012
Blacksburg, Virginia

Keywords: Spontaneous Emission, Fluorescence Lifetime, Photonic Density of States (PDOS), Plasmonic Structures, Self-Assembly, Patterning

Investigating the Modification of Spontaneous Emission using Layer-by-Layer Self-Assembly

Islam Ahmed Ibrahim Youssef Ashry

(ABSTRACT)

The process of spontaneous emission can be dramatically modified by optical micro- and nanostructures. We studied the modification of fluorescence dynamics using a polymer spacer layer fabricated through layer-by-layer (LbL) self-assembly. The advantages of this method are numerous: The self-assembled spacers can possess exceptional smooth surface morphology; The thickness of the spacer can be controlled with nanometer accuracy; And depending on fabrication conditions, the spacer layer is stimuli responsive and its thickness can be dynamically tuned.

This thesis contains three interlinked components. First, we vary LbL spacer layer thickness and explore the change in fluorescence lifetime induced by the modified photonic density of states (PDOS), i.e., Purcell effects. Our experimental results agree well with theoretical predictions based on a classical dipole model, which also yields consistent values for the fluorophores' intrinsic fluorescence lifetime and quantum yield near a dielectric as well as a plasmonic interface. Based on this observation, we further demonstrate that self-assembled fluorophores can be used to probe the modified PDOS near optical micro- and nano-structures.

These results naturally lead to the second component of our research. In particularly,

based on the PDOS-induced changes in fluorescent lifetime, we develop a non-contact method that can measure morphological changes with nanoscale resolution. Our method relies on quantitatively linking fluorophore position with PDOS, and is validated through direct comparison with ellipsometry and atomic force microscopy (AFM) measurements. To demonstrate the potential application of this method, we investigated the swelling/deswelling of LbL films induced by pH changes. Our results indicate significant difference between a LbL film composed of a single polymer monolayer and a LbL film with 3 monolayers. Such stimuli-responsive polymers can be used to construct active and tunable plasmonic nano-devices. As a proof-of-principle demonstration, we experimentally confirm that it is possible to utilize the swelling/deswelling behavior of stimuli-responsive films to dynamically control the separation between Au nanoparticles and Texas Red (TR) dyes. This result is based on the strong correlation of TR fluorescence lifetime and nanoparticles-TR separation.

Finally, we investigate the impact of different lithography processes on the fluorescence properties of self-assembled fluorophores. We consider three methods: direct fluorophore patterning through ultraviolet (UV) ablation, focused ion beam (FIB) milling of self-assembled fluorophores, and self-assembly of fluorescent materials over plasmonic nano-patterns.

To my family and my country

Acknowledgments

First and foremost I would like to express my special appreciation and thanks to my advisor Dr. Yong Xu, for giving me the great opportunity to join his group which is full with amazing frontier research activities and great people. I appreciate all his contributions of ideas, time, and funding to make my Ph.D. His logical way of thinking and his wide knowledge have been of great value for me. I am also thankful for the excellent example he has provided as a successful researcher and professor. I hope that I could be as lively, enthusiastic, and energetic as Dr. Xu and to someday be able to make research in different areas as well as he can.

Let me also say ‘thank you’ to my Egyptian advisor, Dr. Ali Okaz, for his continuous support during both of my M.Sc. and Ph.D. degrees. His guidance helped me a lot especially during the writing of this thesis.

I wish to express my warm and sincere thanks to Professor Randy Heflin for providing a full access to his lab facilities. Every discussion with him is always useful, especially in the project of swelling/deswelling behavior of LbL films. I am also grateful to him because my knowledge on optics greatly expanded from his intensive class: “Intermediate Optics”.

My great gratitude is also given to Dr. Hans Robinson for his prompt help and advice, knowledge on chemical physics, as well as some personal conservations every times we met. I also wish to thank him for training me to use e-beam evaporation technique and for solving many obstacles related to self-assembly above plasmonic materials.

I wish to thank the members of my dissertation committee: Drs. Yong Xu, Anbo Wang,

Sedki Riad, Gray Pickrell, Randy Heflin, and Ali Okaz for generously offering their time, support, and guidance throughout the preparation and review of this document.

I cannot forget Ishac Kandas for supporting me during the hard times in my Ph.D. life. He sacrificed a lot of his time to encourage and help me. He is really the best friend for me.

Further gratitude is for all of my colleagues and friends: Dr. Baigang Zhang, Chalongrat Daengngam, Peng Lu, Xiangyu Wei, Aram Lee, Jihaeng Yi, Kathy Wang, and Jeong-Ah Lee for continual help on the laboratory work and unforgettable friendships.

I will forever be thankful to the people of the Department of Mathematical and Physical Engineering, Alexandria University, Egypt, especially my former M.Sc. advisors: Drs. Ali Okaz, Mustafa Hussen, and Mohamed Keshk. They were and remain my best role model for a scientist, mentor, and teacher.

Special thanks to the VT-MENA program for the financial support and continual care throughout my graduate study in the US. I also wish to thank Dr. Sedki Riad for supporting me in all of the problems I faced during my Ph.D.

I owe my loving thanks to my wife Youmna Daw. She has lost a lot due to my research abroad. Without her encouragement, support, quiet patience, and understanding it would have been impossible for me to finish this work. I appreciate her patience to listen to all of the details and problems in my research even if she is not interested in the subject at all. Also, I owe my loving thanks to my son, Omar Islam Ashry, who has been the most valuable gift in my life. I hope you always know how much I love you.

Last but not the least, my deep gratitude is given for my mother, father, brother, and sister for their unconditional love, support and endless encouragement even from the far side of

the globe. Every personal and academic issue was shared with them. With their unceasing love, my journey to the Ph.D. has never been lonely.

Contents

List of Figures

Chapter 1

Introduction

Spontaneous emission is a fundamental physical process that serves as a basic cornerstone of photonics technology. According to the quantum theory [1], spontaneous emission occurs when fluorophores such as atoms, molecules, or nanocrystals undergo transition from excited states to the ground state.

It was Purcell who first pointed out that the rate of spontaneous emission depends on the photonic density of states (PDOS) [2,3]. The underlying rationale is simple. Image a case where there is no optical mode at the emission wavelength. As a result, the coupling between fluorophores and photons becomes impossible, since no valid optical mode exists. Under this idealized scenario, the spontaneous lifetime approaches infinity, and the fluorophores will remain on the exited state forever. Experimentally demonstrating the PDOS-induced lifetime modification, however, is not easy. In particular, in order to achieve a significantly modified emission rate, we need to fabricate optical device with dimensions on the order of the emission wavelength. For fluorophores that emit light in or near the visible spectral range, this requires us to pattern dielectric or metallic structures with micro- or even nanoscale accuracy.

In 1966, Drexhange started the first experimental study on the modification of the spontaneous emission rate of Eu^{3+} ions using planar metallic interfaces [4]. The

enhancement of the spontaneous emission rate using a cavity was later verified by Goy *et al.* [5]. It was also noticed that optical cavities can be used to inhibit the decay rate [6]. Since then, the modification of spontaneous emission rate has been experimentally or theoretically investigated using different optical structures such as photonic crystals (PCs) [7,8], metamaterials [9], and plasmonic nanostructures [10,11].

1.1 Motivation

Spontaneous emission serves as the foundation of some of the most important applications of photonics industry, with examples such as solar cells [12], illumination [13], optical communications [14], displays [15], lasers [16], light emitting diodes (LEDs) [17], and quantum-information systems [18]. Increasing the spontaneous emission rate is highly desirable in some applications. For instance, in LEDs, which are mainly use spontaneous emission to produce light, their performance is usually limited by the unfortunate fact that a large amount of spontaneous emission are trapped within and cannot be easily "extracted" from the light emitting materials. Therefore, enhancing the spontaneous emission rate can improve the performance, such as the quantum efficiency, of the LEDs [19].

At the same time, reducing the spontaneous emission rate can also be very useful for certain applications. For example, the conversion efficiency of solar cells can be reduced a lot due to spontaneous emission. In this case, it is possible to improve the efficiency of solar cells through spontaneous emission inhibition [20]. These two examples show that there is a strong motivation to control the spontaneous emission process.

1.2 Research Objectives

This research aims to investigate the modification of spontaneous emission using a layer-by-layer (LbL) self-assembly technique. More specifically, we aim to accomplish the following research objectives.

1- Experimentally study the modification of fluorescence dynamics using LbL polymer spacers with different, but fixed, layer thickness. Compare the experimentally measured fluorescence lifetime with the theoretical predictions obtained using a classical dipole model. Finally, develop a procedure that can probe the modified PDOS near optical micro- and nano-structures using experimentally extracted intrinsic fluorescence lifetime and quantum yield.

2- Develop a non-contact method based on PDOS induced lifetime changes and apply this method to investigate the swelling / deswelling behaviors of LbL films with nanoscale resolution.

3- Characterize the impact of different lithography processes on the fluorescence properties of self-assembled LbL polymeric thin films.

1.3 Thesis Organization

This dissertation is organized as follows:

Chapter 2: Background and Related Work

In this Chapter, we briefly discuss some key topics that are directly related to the research presented in this thesis. In particular, we summarize the theoretical background for fluorescence emission and the basics of the time-correlated single photon counting (TCSPC) system used for fluorescence lifetime measurements. We then briefly review

the basics of semiconductor quantum dots (QDs). Afterwards, the process of LbL self-assembly is discussed to show its advantages and report some examples for using it through the modification of fluorescence dynamics. Finally, we provide some related work on controlling fluorescence dynamics using planar structures, PCs, and plasmonic structures.

Chapter 3: Theoretical Models of Spontaneous Emission near Planar Structures

In this Chapter, we review the classical and the quantum framework for the analysis of spontaneous emission near a planar structure. The equivalence between the two models is demonstrated.

Chapter 4: Probing the Photonic Density of States Using Layer-by-Layer Self-Assembly

This Chapter starts with describing how charged fluorophores can be self-assembled above dielectric and plasmonic substrates. Furthermore, we demonstrate how simply LbL self-assembly can be used to control the distance between the self-assembled fluorophores and the underlying substrates. We then describe the experimental setup used to measure fluorescence decay and the calculation of fluorescence lifetime. Finally, we describe how to use the changes in fluorescence lifetime to quantify the modification of PDOS by the surrounding dielectric / metallic structures.

Chapter 5: Characterizing Nanoscale Morphological Changes using Purcell Effects

This Chapter presents our approach of using PDOS induced lifetime changes, i.e. Purcell effect, to measure the morphological changes with nanoscale resolution of LbL films. This approach is used to characterize the swelling/deswelling behavior of a single polymer monolayer and a LbL film with 3 monolayers. Finally, we compare the thickness

measurements obtained using our approach with those measured using atomic force microscopy (AFM). We also report a preliminary study on using these swellable films to construct active and tunable plasmonic nano-devices.

Chapter 6: Characterizing the Impact of Micro- and Nano-lithography on the Fluorescence Dynamics of Self-Assembled Fluorophores

In this Chapter, we investigate the impact of various lithographical processes on the fluorescence properties of various fluorophores. We first study the impact of evaporating and etching aluminum mask on two different self-assembled fluorophores. Next, we study the impact of UV ablation and FIB milling on self-assembled fluorescent polymers. Finally, we study the effect of self-assembly of fluorophore over plasmonic nano-patterns on their fluorescence dynamics.

Chapter 7: Summary and Future work

In this Chapter, we highlight our theoretical and experimental results on quantifying fluorescence emission near dielectric and plasmonic structures, the probing of PDOS, the study of swellable polymers, and the initial development of tunable and active plasmonics. Finally, we provide a brief outlook concerning possible future development.

References

1. R. Loudon, *The Quantum Theory of Light*, 3rd edition, (Oxford University Press, New York, 2000).
2. L. Novotny, and B. Hecht, *Principles of Nano-Optics*, 1st edition, (Cambridge University Press, New York, 2006).
3. E. M. Purcell, Phys. Rev. **69**, 681 (1946).
4. K. H. Drexhage, M. Fleck, F. P. Shafer, and W. Sperling, Phys. Chem. **20**, 1176 (1966).
5. P. Goy, J. M. Raimond, M. Gross, and S. Haroche, Phys. Rev. Lett. **50**, 1903 (1983).
6. D. Kleppner, Phys. Rev. Lett. **47**, 233 (1981).
7. E.Yablonovitch, Phys. Rev. Lett. **58**, 2059 (1987).
8. S. John, Phys. Rev. Lett. **58**, 2486 (1987).
9. Z. Jacob, J. Y. Kim, G. V. Naik, A. Boltasseva, E. E. Narimanov, and V. M. Shalaev, Applied Physics B-Lasers and Optics. **100**, 215 (2010).
10. Vamsi. K. Komarala, Yury. P. Rakovich, A. L. Bardley, Stephen J. Byrne, Yurii K. Gun'ko, N. Gaponik, and A. Eychmüller, Applied Physics Letters. **89**, 253118 (2006).
11. C. W. Chen, C. H. Wang, C. M. Wei, and Y. F. Chen, Applied Physics Letters. **94**, 71906 (2009).
12. M. Grätzel, Nature. **414**, 338 (2001).
13. E. F. Schubert, and J. K. Kim, Science. **308**, 1278 (2005).
14. Y. Suematsu, and S. Arai, IEEE J. Sel. Top. Quant. Electron. **6**, 1436 (2000).
15. K. Ziemelis, Nature. **399**, 408 (1999).

16 J. M. Senior, *Optical Fiber Communications*, 2nd edition, (Prentice, Harlow, 1992).

17 H. Mabuchi, and A. C. Doherty, Science. **298**, 1372 (2002).

18 S. Noda, M. Fujita, and T. Asano, Nature Phot. **1**, 449 (2007).

19 M. Boroditsky, and E. Yablonovitch, "Spontaneous Emission Engineering in Light Emitting Diodes," CLEO (1997).

20 B. Ellis, T. Sarmiento, J. Harris, and J. Vuckovic, "High Efficiency Solar Cells based on Spontaneous Emission Inhibition in Photonic Crystals," CLEO (2009).

Chapter 2

Background and Related Work

In this Chapter, we first review the conceptual framework of fluorescence emission and discuss the basic characteristics of fluorophores. Afterwards, we present the basic concept behind TCSPC, which is used to measure fluorescence lifetime. Then, we describe the process of LbL electrostatic self-assembly, which has the advantage of being capable of generating conformal films with sub-nm thickness control on almost any surface with relative ease. Finally, we summarize prior literature related to our work on spontaneous emission modification.

2.1 Basic Concepts of Fluorescence Emission

Spontaneous emission refers to the process in which fluorophores such as atoms, molecules, dyes, or QDs return to lower energy states and spontaneously emit a photon. The spontaneous emission process is usually illustrated using the energy band diagram in Fig. (2.1.1). In this figure, ground state, first excited state, and second excited state are depicted by S_0, S_1, and S_2, respectively. At each of these states, the fluorophores can occupy any of energy sub-levels, depicted by 0, 1, 2, etc.

Normally, fluorophores occupy the lowest energy level (S_0 in sub-level 0 in Fig. (2.1.1)), i.e., the ground state. When light from an external source is absorbed by the fluorophore,

it can be excited to one of the excited states. Afterwards, the fluorophore loses some of its energy and relaxes to the lowest sub-level of S_1. Fluorophore may then directly return to S_0 and produce a photon to conserve energy. This process is called spontaneous emission.

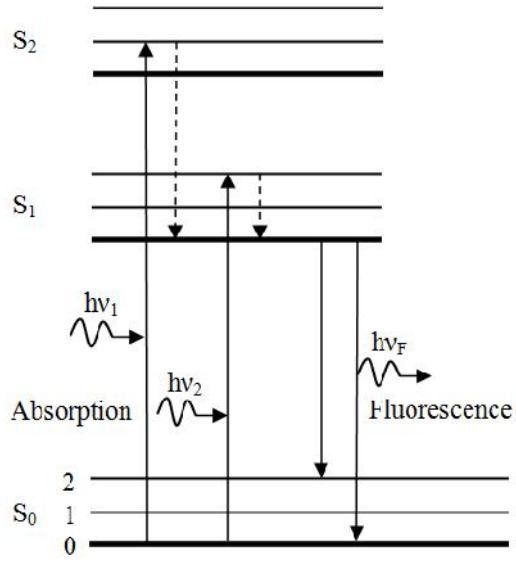

Figure 2.1.1: Energy band diagram which describes the fluorescence phenomenon.

The quantum yield and the fluorescence lifetime are two important characteristics of a fluorophore. The total decay rate from the excited state to the ground states is the sum of the radiative decay rate, which is associated with light emission, and nonradiative decay rate. For any fluorophore, its quantum yield quantifies the efficiency of the light emission process. Specifically, it is defined as the ratio of the radiative decay rate to the total decay rate (i.e., the radiative plus the nonradiative decay rate). This value is always less than unity. Each fluorophore is characterized by its τ, which is defined as the average time the fluorophore stays in the excited state before it returns back to the ground state [3].

2.2 Time-Correlated Single Photon Counting

One of the best methods to accurately measure the time dependence of fluorescence decay is TCSPC. In this approach, the fluorophores are excited using a pulsed light source with short time duration (e.g., < 1ns) and high repetition rate (e.g., >1 MHz). After each pump pulse, the fluorophores emit fluorescent signals with time dependence as shown in Fig. (2.2.1).

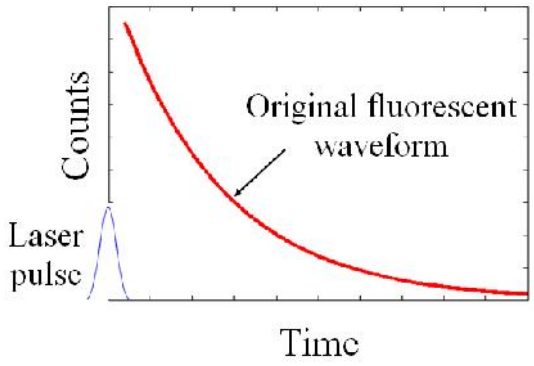

Figure 2.2.1: Typical fluorescence decay of fluorophores when excited using picosecond or femotosecond laser.

For weak fluorescent signals, it is very difficult to record the whole fluorescent waveform after a single laser pulse, and TCSPC is developed to address this difficult challenge. In TCSPC system, one typically uses a highly sensitive detector to capture the weak fluorescent signal. A few examples are photomultiplier tube (PMT), single photon avalanche diode (SPAD), or micro channel plat (MCP). For weak fluorescent signals, the probability of fluorescence photon detection is typically less than one. However, by repeating this photon counting process for a large number of pulses pump light, it is possible to accurately capture the weak fluorescent signal. Fig. (2.2.2) illustrates how the

histogram for the fluorescence decay can be captured. Specifically, we record the time difference between the excitation pulse and the time at which the fluorescent photon is captured. Then we divide the time duration between two sequential pump pulses into numerous digital channels and store the photon counts in appropriate time slots. Afterwards, the histogram is collected from the final readings of all memory cells. After a sufficiently long period of data collection the histogram can accurately represent the time dependence of fluorescence decay.

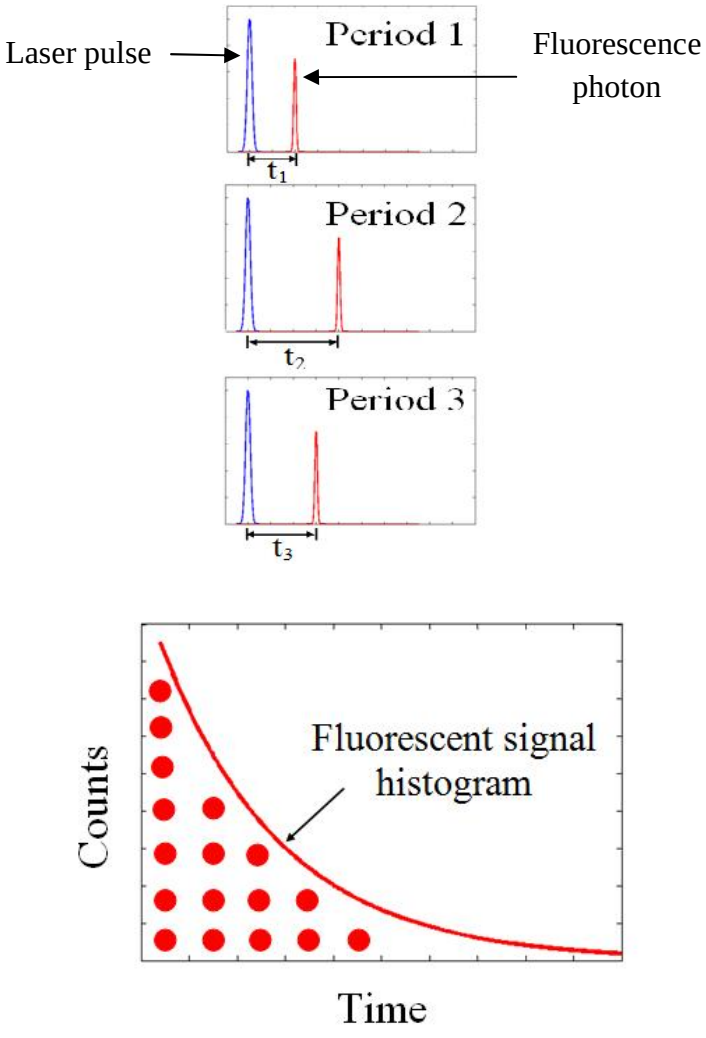

Figure 2.2.2: Typical fluorescence decay histogram.

The time difference between the excitation pulse and the fluorescence photon detection can be measured using specialized electronic devices [3]. When the pump pulse starts to excite the fluorophores, an electronic trigger signal is sent simultaneously to a constant function discriminator (CFD) that record the arrival time of the pulse. Afterwards, the trigger signal is directed to a time-to-amplitude converter (TAC) that generates a voltage increases linearly with time in nanosecond scale. A parallel channel receives a pulse when the single photon is detected and another CFD is used to determine the arrival time of the pulse and sends signal to stop the voltage increase. The voltage of the TAC now is proportional to the time difference between the excitation and emission signals. Finally, this voltage is converted to a numerical value using analog-to-digital converter to be stored as a single event with the measured time difference. The fluorescence waveform can be produced after repeating this process numerous times.

2.3 Semiconductor Quantum Dots

QDs are semiconductor nanocrystals and their optical characteristics can be adjusted by changing their compositions, sizes and shapes [4-7]. As shown in Fig. (2.3.1), when the radius of the QD is larger than the exciton Bohr radius, the exciton acts as if it is free and the original energy levels are not changed. However, when the radius of the QD becomes smaller than the exciton Bohr radius, the crowding of electrons leads to quantum confinement [8]. Therefore, the original energy levels are splitted into sublevels with smaller gaps between them. The quantized energy levels can be described using particle in a box which demonstrate the reason of why QD optical properties depend on their sizes. Typically, if the size of the QD is less than 10 nm, the quantum confinement effect

dominates and the fluorescence wavelength is determined by the QD size [8].

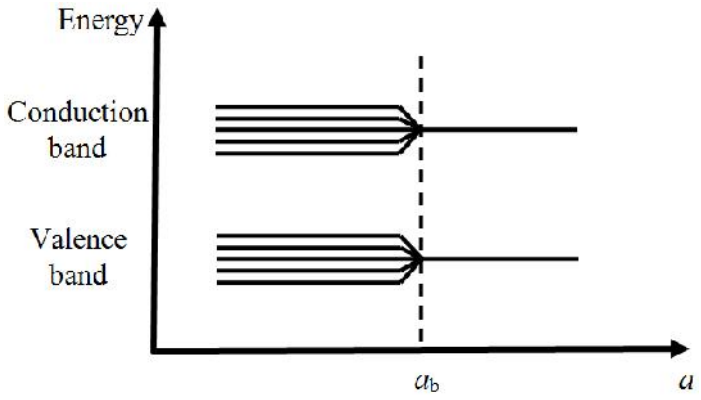

Figure 2.3.1: Quantum confinement effect in small QDs. The horizontal axis represents the radius of the QD, a, and a_b is the exciton Bohr radius.

When QDs are excited, excitons are formed by transferring electrons to the conduction band and leaving holes in the valence band. Afterwards, the excited electrons return to the valence band through electron-hole recombination. Simultaneously, fluorescence photons are emitted. The energy of the emitted photon, Fig. (2.3.2), is simply the sum of the bandgap between the conduction and valence bands, the confinement energy of the excited electron and hole, and the bound energy of the exciton. As the size of the QD decreases, the wavelength of the fluorescent emitted photon decreases and vice versa [9]. Semiconductor QDs have the same crystal structure as that of the bulk solids. Since the crystal lattice suddenly stops the QD surface, the incomplete bonding structure at the surface forms atomic orbitals called unpassivated orbitals [11]. If the energy of the unpassivated orbital band is within the bandgap of the core, excitons may be captured on such surface defects, which results in decrease of the QD quantum yield. In order to solve this issue, the core of the QD is typically covered with a shell semiconductor layer with

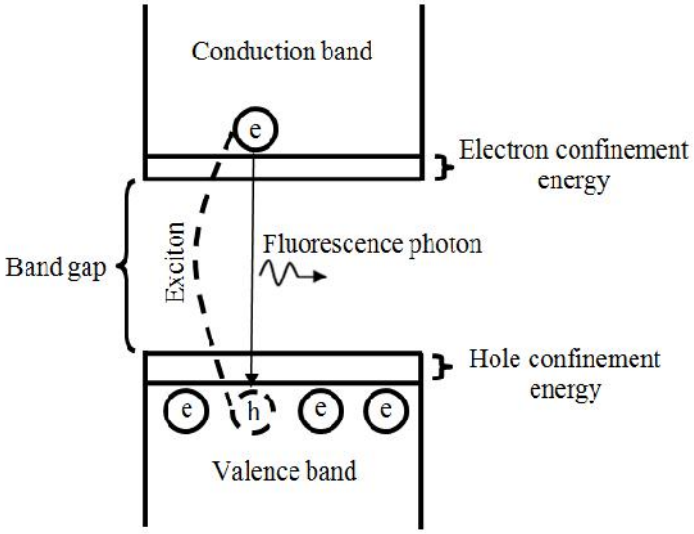

Figure 2.3.2: Fluorescence photon emission from QDs.

larger bandgap and the chemical composition of the core changes suddenly within one atomic layer [8]. Typically the CdSe QD is covered with a higher bandgap ZnS shell layer. Afterwards, the shell layer can also be functionalized with proper surface chemistry without changing the optical properties of the QDs.

Fig. (2.3.3) shows an example for the absorption spectrum of colloidal CdSe/ZnS

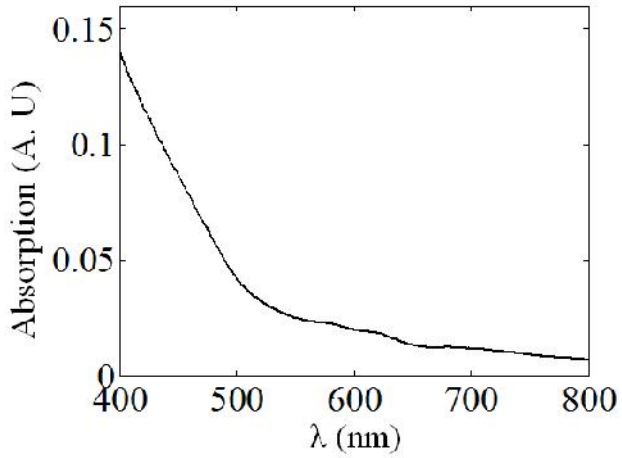

Figure 2.3.3: Absorption spectrum of CdSe/ZnS core/shell QDs.

core/shell QDs (from NN-LABS, emission peak at 621 nm, 5 nm mean diameter) coated with negatively charged mercaptoundecanoic acid ligands.

QDs have found many applications such as solid-state quantum computation [13], biology [14], LEDs [15], and photodetector devices [16].

2.4 Layer-by-Layer Electrostatic Self-Assembly

LbL electrostatic self-assembly, which relies on ionic interaction between polymeric materials to sequentially deposit polymer monolayers, was first reported by Decher *et al.* [17]. More specifically, LbL self-assembly is a process in which positive polymers (polycations) and negative polymers (ploy anions) are adsorbed sequentially from dilute aqueous solution onto a charged solid substrate [18-21]. This process can also be used to adsorb other different charged materials such as, nanoparticles [22], ionic dyes [23], viruses [24], proteins [25], and DNA [26]. The LbL approach has several advantages: First of all, the thin films assembled using this approach can be exceptionally smooth and uniform. By adjusting the number of polymer monolayers, we can also control its thickness with nanometer accuracy. Additionally, LbL self-assembly process can be carried out at room temperature without the need of any sophisticated instrument. Last but not the least, LbL self-assembly is simple, inexpensive, and highly versatile.

Fig. (2.4.1-a) illustrates the deposition procedure for LbL self-assembly. First, a charged substrate, such as a gold film with a negatively charged surface, is immersed in aqueous solution of polycation. Due to the electrostatic interaction, a uniform polycation monolayer grows on the substrate. The self-assembly of the polycation reverse the

surface charge and therefore, the growing of the monolayer is self-terminated regardless of longer dipping time. Typically, the deposition of monolayer requires 2-3 minutes to be completed [27]. Afterwards, the substrate is rinsed thoroughly in deionized (DI) water to remove loosely bound polymers. Then, the substrate is dipped in an aqueous solution containing polyanion to similarly deposit another negatively charged polymeric monolayer on the sample surface through electrostatic interaction. Finally, the sample is rinsed again in DI water in order to remove the excess molecules. This process can be repeated till we build up the desired number of bilayers. Fig. (2.4.1-b) shows a typical polymeric bilayers structure above a charged substrate.

It is also possible to fabricate stimuli-responsive LbL films. For example, with appropriate deposition conditions (i.e., weak polyelectrolytes), we can control the thickness of the self-assembled polymer by changing medium pH values [28-30]. Specifically, we can swell / deswell the polymer film by decreasing or increasing solution pH values.

For the aforementioned swellable films, the pH of the solutions used during the self-assembly process is an important factor in determining the characteristics of the pH-induced swelling/deswelling behavior of LbL films containing weak polyelectrolytes. Current research has shown that LbL films containing Poly (allylamine hydrochloride) (PAH) and assembled at pH > 8.5 can exhibit pH-dependent swelling/deswelling behavior over the pH range of 3.0–10.5 [29]. The dynamical changes of such swellable films are typically investigated using ellipsometry [29], transmission electron microscopy (TEM) [30], and AFM [28]. Unlike common materials such as silica or semiconductor, the thickness of a swellable film can be dynamically changed by

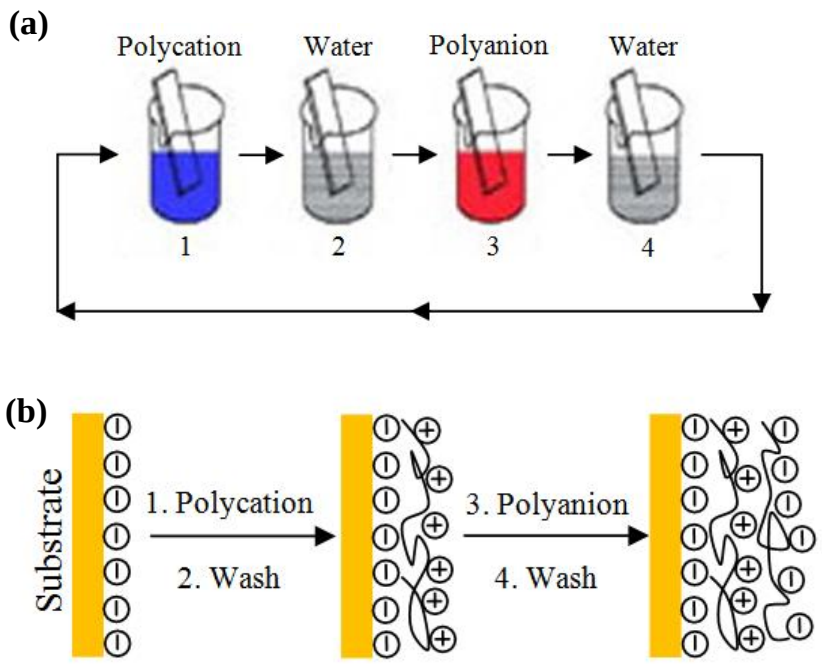

Figure 2.4.1: (a) Steps of LbL self-assembly process, and (b) build-up of LbL polymeric film above a charged substrate.

up to 600% [29]. Given this unique behavior, such swellable polymers have found numerous applications including controlling cell proliferation and attachment [31], drug release [32], and hysteretic gating [30].

Fig. (2.4.2) illustrate the pH-induced swelling / deswelling of LbL films with weak polyelectrolytes LbL films and assembled at pH > 8.5. When the sample is immersed in aqueous solution of pH = 10.5, the polymers lay flat on the substrate and the LbL film deswells. However, when we change the pH of the aqueous solution to 3, the polymers "stand up" and as a result, the thickness of the LbL film dramatically increases.

LbL assembly has been used to study the effect of a large variety of optical micro-/nano-structures on the spontaneous emission lifetime of various fluorophores. Krishanu Ray, *et al.* [33], for example, used the method of LbL assembly to control the distance between

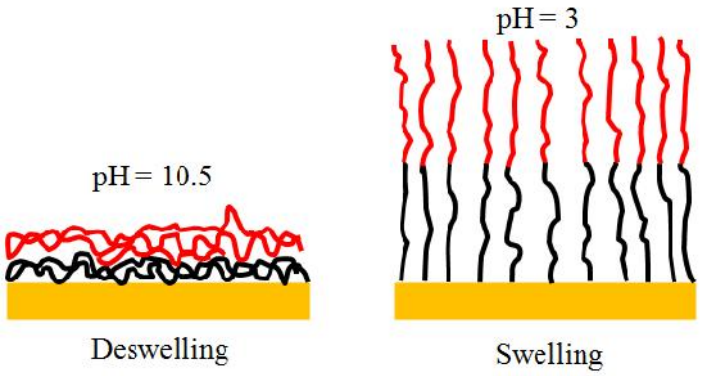

Figure 2.4.2: pH-induced swelling/deswelling behavior of weak polyelectrolytes LbL films preassembled at pH > 8.5.

fluorescent dyes and a planar silver substrate. They found that the fluorescence dynamics of the assembled dyes depends on the LbL film thickness. Another example is Ref. 34. In this work, the authors controlled the distance between CdSe QDs and gold nanoparticles by changing the number of bilayers of LbL film. They found that the QDs luminescence can be significantly enhanced when the distance between the QDs and the gold nanoparticles is very small (< 25 nm), provided that the excitation wavelength is identical to the plasmonic resonance of the gold nanoparticles.

2.5 Modification of Fluorescence Dynamics

The fluorescence dynamics of a fluorophore can be modified by engineering the micro- or nanostructures in its vicinity. This modification is due to the change of the PDOS, i.e., Purcell effects. To date, this phenomenon has been theoretically or experimentally investigated using, different optical micro- and nano-structures such as, planar substrates [35], photonic crystals (PCs) [36], microcavities [37], plasmonic materials [38], and

metamaterials [39]. In this section, we briefly review some important examples of optical structures used for the control of fluorescence dynamics.

2.5.1 Planar Structures Based Fluorescence Modification

The first experimental study of fluorescence lifetime modification is dated back to Drexhange [40], who studied the impact of a metallic mirror on the spontaneous emission lifetime of Eu^{3+} ions. In this method, Langmuir-Blodgett films [41,42] were formed by depositing different number of fatty acid monolayers on the metal substrate. Afterwards, a layer of Eu^{3+} ions was placed on the topmost layer such that the separation between the fluorophores and the substrate was obtained by controlling the monolayer number. The Eu^{3+} ions were then excited and their fluorescence lifetime was measured using samples with different ions / substrate distances. It was observed that at large separations from the metallic substrate, the fluorescence lifetime was oscillatory, while at small distances it monotonically decreased towards zero.

Jia-Yu Zhang *et al.* [43] used a semiconductor planar Si/SiO_2 structure to modify the spontaneous emission lifetime of CdSe/CdS core/shell QDs. In their work, SiO_2 thermal film was used as a spacer between the Si substrate and the QDs. The QDs were assembled above the SiO_2 film by using spin coating of a dilute solution of the QDs in toluene with 1 % PMMA upon the SiO_2 film. They concluded that the modification of fluorescence lifetime of the used QDs can be described by the classical single dipole model near planar interface [35].

Metal-enhanced fluorescence from sulforhodamine B dye has been studied by Krishanu Ray *et al.* [44]. In this study, LbL self-assembly was used to control the distance between the used dye and a silver island film. The steady-state and time-resolved fluorescence

spectral property of the sulforhodamine B dye were calculated as a function of the metal-fluorophore distance. This distance was controlled by changing the number of bilayers of the self-assembled film. They found that the maximum enhancements of fluorescence happens when the LbL film thickness is about 8-9 nm.

Last but not the least, the quantum efficiency of a single fluorescent molecular dipole was calculated by using a scanning probe technique as described in [45]. An inverted microscope combined with a shear-force scanning probe was used to specifically control the distance between the fluorescent molecule and a movable silver mirror. From the modification of the lifetime and radiated intensity of the molecule due to the mirror position, the authors can extract the quantum efficiency of the molecule.

2.5.2 Photonic Crystals Based Fluorescence Modification

Solid state theory clearly demonstrates that a periodically arranged atomic lattice can produce an electronic bandgap that can eliminate any electronic state within this bandgap. The concept of PCs is directly based on this well-known result.

More specifically, PC is the optical analog of solid state crystals, where periodically arranged atoms and molecules are replaced by dielectric materials with spatially periodic index variations. If the difference between the dielectric constants of the materials is sufficiently high and the material absorption is sufficiently low, the reflection and refraction of light at various interfaces can produce a photonic bandgap that can completely prohibit light propagation in all three dimensions.

As a result, as long as emission wavelength is within such a PC with 3D bandgap, we can completely inhibit spontaneous emission in such a structure.

Recently, control of spontaneous emission by 2D and 3D PCs has been demonstrated successfully [46−49].

An example of 2D PCs is the triangular lattice of air holes in a substrate of high dielectric constant, shown in Fig. (2.5.1). Fig. (2.5.2) shows the band structure for this lattice at r / a = 0.48 and ε = 13, where r is the hole radius, a is the lattice constant, and ε is the dielectric constant of the substrate. This band structure is calculated using the MIT package [50].

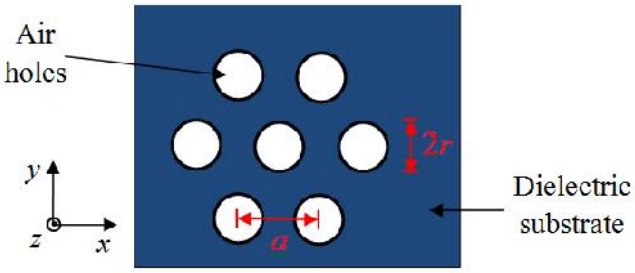

Figure 2.5.1: A view from above to two-dimensional triangular PC of air holes in dielectric substrate with infinite length in z direction.

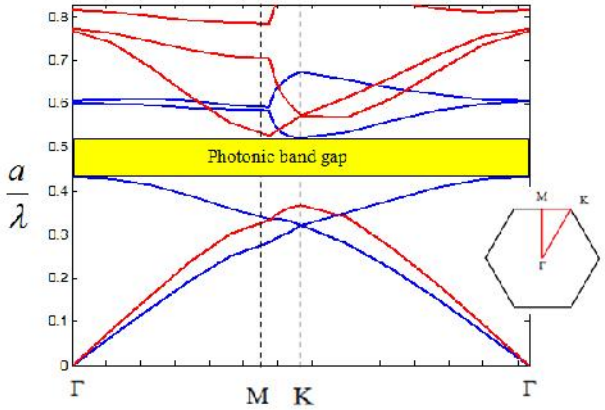

Figure 2.5.2: The photonic band structure for the modes of the triangular two-dimensional PC of air holes in dielectric substrate. The blue bands represent TM modes and the red bands represent the TE mode. The inset shows the selected path for the Brillouin zone.

Ref. 48 provides a good example of spontaneous emission control using 2D photonic bandgap [48]. In this work, a series of samples were prepared on a GaInAsP two-dimensional triangular PC slab with various lattice constant, *a*, such that the photonic bandgap shifts to longer wavelengths with the increase of *a*. This PC contains a single quantum-well light emitting layer. When the photonic bandgap covers the emission wavelength region, the spontaneous emission lifetime increases compared with that observed without the photonic bandgap effect. This means the spontaneous emission was inhibited in the in-plane direction due to the photonic bandgap effect and consequently, the emission efficiency in vertical modes also increases.

Another example for inhibiting the spontaneous emission in QDs using two-dimensional PC is reported in Ref. [49]. In this work, a GaAs slab of 200 nm thickness that contains InAs QDs incorporated within a two-dimensional triangular lattice PC with air-holes. When the photonic bandgap of the PC includes the whole emission wavelengths of the QDs, the fluorescence lifetime of the QDs was found to be 15-fold longer than that on a reference sample without any PC structure. This is due to the inhibition of the emission channel in the photonic crystal plane. Simultaneously, the vertical emission efficiency was enhanced with respect to that measure on the reference sample.

Three-dimensional finite difference time domain (FDTD) method has been used by A. Femius Koenderink *et al*. to characterize the modification of fluorescence lifetime of a single emitter as a function of its distance from a two-dimensional PC slab. For an emitter located at the center of the PC membrane, the fluorescence lifetime increases by a factor of 7 in the bandgap with respect to its fluorescence lifetime in vacuum. However, on the edges of the bandgap, oscillatory emission enhancement was observed with a maximum

larger than a factor of 15 as compared with the vacuum emission. It was observed that as the distance between the emitter and the center of the PC increases, the inhibition and enhancement behavior are reduced in size.

2.5.3 Plasmon Based Fluorescence Modification

A defining feature of noble metals such as gold and silver is the existence of surface plasmons, which are defined as the electron-density oscillations that exist near the metal-dielectric interface [8]. Under certain conditions [8], photons can be coupled with surface plasmons and propagate along the interface. The existence of surface plasmons often results in strongly enhanced optical fields near the meta-dielectric interface.

The frequency of plasmonic resonance also depends on the shape and size of the metallic nanostructures [52].

Numerous experimental and theoretical studies have demonstrated that plasmonic nanostructures can have significant impact on fluorescence dynamics. In this section, we show several representative examples in current literature.

Alexandre G. Brolo *et al.* [53]. used focused ion beam (FIB) to fabricate seven nanoholes arrays on gold substrate. These arrays were fabricated with different periodicities and the average diameter of these holes was 100 nm. It was found that the plasmonic resonance through transmission of these arrays could be tuned by changing the periodicity of the arrays. The arrays were then spin-coated with polystyrene film which contains fluorescent dye. Fixed wavelength laser source was used to excite the dye such that, the laser light passed first through the nanoholes and then excited the dye, Fig. (2.5.3). It was observed that when the wavelength of the laser source matched the plasmonic resonance

of one of the nanoholes arrays, strong fluorescence enhancement could be collected from the used dye relative to that obtained from identical films coated onto glass slides.

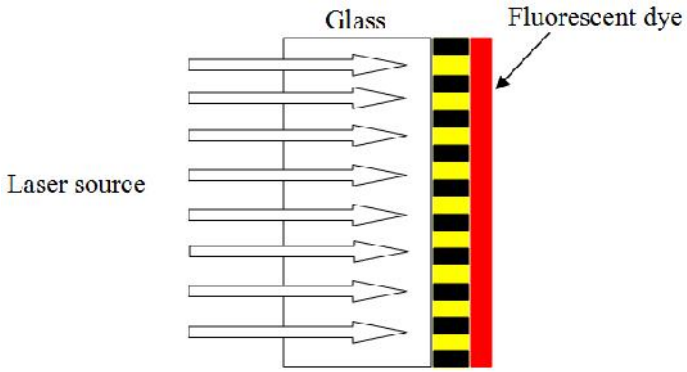

Figure 2.5.3: Excitation of fluorescent dye through plasmonic nanoholes.

Another exmple is the work by Jung-Hoon Song *et al.* [54], which shows enhanced fluorescence intensity from QDs placed near plasmonic nanostructure. The plasmonic material used in this paper consisted of lithographically patterned periodic arrays of silver islands. Using the standard transmission/reflection setup to measure the plasmonic resonance of this structure, it was found that the wavelength of the plasmonic resonance can be shifted by changing the lattice constant of the periodic structure. The array was fabricated by first dispersing colloidal CdSe/ZnS in poly (methyl methacrylate) (PMMA) thin films. Afterwards, two-dimensional silver-particle array was formed by using the PMMA as a resist for electron-beam lithography, followed by etching and evaporating silver film. The produced structure is shown schematically in Fig. (2.5.4). It was observed that when the plasmonic resonance is tuned to match the fluorescence wavelength of the QDs, the fluorescence intensity can be enhanced by a factor of 50 relative to the case of unpatterned area.

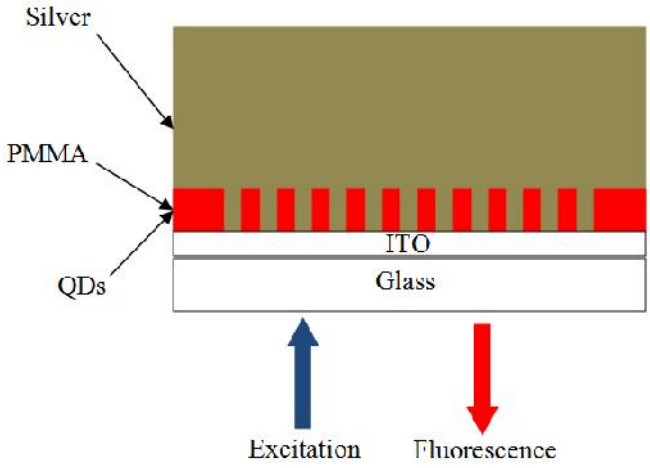

Figure 2.5.4: Schematic for exciting QDs above silver plasmonic structure.

Colloidal gold nanoparticles can be used to enhance photoluminescence. For example, Olga Kulakovich *et al.* [55]. control the emission intensity produced by placing QDs near gold nanoparticles. They self-assmbled a monolayer of negatively charged gold nanoparticles on glass substrate covered with polycations. These gold colloids have a plasmonic resonance at 550 nm which can be used to excite CdSe/ZnS QDs. Afterwards, they alternately deposited LbL film which consists of polydiallyldimethylammonium chloride (PDADMAC, polycation) and sodium polystyrene sulfonate (PSS, polyanion) to act as a spacer between the gold nanoparticles and the QDs. Finally, negatively charged CdSe/ZnS QDs were deposited on the PDADMAC topmost layer. These QDs were excited using a light of 550 nm wavelength which matches the plasmonic resonance of the gold nanoparticles. It was found that at extremely small distance(<5 nm between the QDs and gold nanoparticles), the fluorescence intensity of the QDs decreased due to quenching effect. However, if the spacing between QDs and the gold nanoparticles is 11 nm, the florescence intensity was enhanced by a factor of 5 relative to the intensity of QDs assembled above the glass slide without gold nanoparticles at spacing. This

enhancement can be attributed to the enhanced pump light due to the plasmonic gold nanoparticles. For larger spacing (QDs-nanoparticle distances exceeding 11 nm), the QD fluorescence intensity decreased gradually because of the reduced plasmonic enhancement.

References

1. M. Massimi, *Pauli's Exclusion Principle: the Origin and Validation of a Scientific Principle*, 1st edition, (Cambridge University Press, New York, 2005).
2. M. Kasha, Disc. Faraday Soc. **9**, 14 (1950).
3. J. R. Lakowicz, *Principles of Fluorescence Spectroscopy*, 3rd edition, (Springer, New York, 2006).
4. A. I. Ekimov, and A. A. Onushchenko, JETP Letters. **34**, 345 (1982).
5. S. Neeleshwar, C. L. Chen, C. B. Tsai, and Y. Y. Chen, Phys. Rev. B. **71**, 201307 (2005).
6. I. Moreels, K. Lambert, D. Smeets, D. D. Muynck, T. Nollet, J. C. Martins, F. Vanhaecke, A. Vantomme, C. Delerue, G. Allan, and Z. Hens, ACS Nano. **3**, 3023 (2009).
7. R. Heitz, S. Rodt, A. Schliwa, and D. Bimberg, Phys. Status Solidi (B). **238**, 273 (2003).
8. L. Novotny, and B. Hecht, *Principles of Nano-Optics*, 1st edition, (Cambridge University Press, New York, 2006).
9. B. O. Dabbousi, J. Rodriguez-Viejo, F. V. Mikulec, J. R. Heine, H. Mattoussi, R. Ober, K. F. Jensen, and M. G. Bawendi, J. Phys. Chem. B. **101**, 9463 (1997).
10. J. Brandrup, and E. H. Immergut, *Polymer Handbook*, 2nd edition, (Wiley, New York, 1966).

11. M. S. Andrew, and S. Nie, Acc. Chem. Res. **43**, 190 (2010).
12. S. Pokrant, and K. B. Whaley, the Europ. Phys. Journal D. **6**, 255 (1999).
13. D. Loss, and D. P. DiVincenzo, Phys. Rev. A. **56**, 120 (1998).
14. R. E. Bailey, A. M. Smith, and S. Nie, Physica E: Low-dimensional Systems and Nanostructures. **25**, 1 (2004).
15. N. Park, T. Kim, and S. Park, Appl. Phys. Lett. **78**, 2575 (2001).
16. S. Maimon1, E. Finkman1, G. Bahir1, S. E. Schacham, J. M. Garcia, and P. M. Petroff, Appl. Phys. Lett. **73**, 2003 (1998).
17. G. Decher, I. J. D. Hong, and J. Schmitt, Thin Solid Films. **210**, 831 (1992).
18. G. D. Kounoike, Science. **277**, 1232 (1997).
19. F. Caruso, R. A. Caruso, and H. Moehwald, Science. **282**, 1111 (1998).
20. K. Ariga, J. P. Hill, and Q. Ji, Chem. Phys. **9**, 2319 (2007).
21. A. Tulpar, Z. Wang, C-H. Jang, V. Jain, J. R. Heflin, and A. Ducker, Nanotechnol. **20**, 155301 (2009).
22. N. Higashi, T. Takagi, and T. Koga, Polymer Journal. **42**, 95 (2010).
23. P. S. Grant, and M. J. McShane, IEEE Sensor Journal. **3**, 139 (2003).
24. P. J. Yoo, K. T. Nam, J. Ql, S-K Lee, J. Park, A. M. Belcher, and P. T. Hammond, Nature. **234**, 234 (2006).
25. F. Caruso, and H. Möhwald, J. Am. Chem. Soc. **121**, 6039 (1999).
26. K. Ren, J. Ji, and J. Shen, Biomaterials. **27**, 1152 (2006).
27. A. Garg, R. M. Davis, C. Durak, J. R. Heflin, and H. W. Gibson, J. Appl. Phys. **104**, 053116 (2008).
28. J. A. Hiller, and M. F. Rubner, Macromolecules. **36**, 4078 (2003).

29. K. Itano, J. Choi, and M. F. Rubner, Macromolecules. **38**, 3450 (2005).
30. D. Lee, A. J. Nolte, A. L. Kunz, M. F. Rubner, and R. E. Cohen, J. Am. Chem. Soc. **128**, 8521 (2006).
31. D. Mendelsohn, S. Y. Yang, J. Hiller, A. I. Hochbaum, and M. F. Rubner, J. Biomacromolecules. **4**, 96 (2003).
32. A. J. Chung, and M. F. Rubner, Langmuir. **18**, 1176 (2002).
33. K. Ray, R. Badugu, and J. R. Lakowicz, Chem. Mater. **19**, 5902 (2007).
34. O. Kulakovich, N. Strekal, A. Yaroshevich, S. Maskevich, S. Gaponenko, I. Nabiev, U. Woggon, and M. Artemyev, ACS Nanolett. **2**, 1449 (2002).
35. R. R. Chance, A. Prock, and R. Silbey, Adv. Chem. Phys. **37**, 1 (1978).
36. G. Liu, Y. Liao, S. Ma, Y. Shen, and Z. Ye, J. Opt. Soc. Am. B. **27**, 1942 (2010).
37. D. Englund, D. Fattal, E. Waks, G. Solomon, B. Zhang, T. Nakaoka, Y. Arakawa, Y. Yamamoto, and J. Vučković, Phys. Rev. Lett. **95**, 13904 (2005).
38. V. K. Komarala, Y. P. Rakovich, A. L. Bardley, S. J. Byrne, Y. K. Gun'ko, N. Gaponik, and A. Eychmüller, Applied Physics Letters. **89**, 253118 (2006).
39. Z. Jacob, J. Y. Kim, G. V. Naik, A. Boltasseva, E. E. Narimanov, and V. M. Shalaev, Applied Physics B-Lasers and Optics. **100**, 215 (2010).
40. K. H. Drexhage, *Progress in Optics*, E. Wolf, ed. (North-Holland, Amesterdam, 1974).
41. K.B. Blodgett, J. Am. Chem. Soc. **57**, 1007 (1935).
42. H. Kuhn, J. Chem. Phys. **53**, 101 (1970).
43. J. Zhang, X. Wang, and M. Xiao, Optics Letters. **27**, 1253 (2002).

44. K. Ray, R. Badugu, and J. R. Lakowicz, Chemistry of Materials. **19**, 5902 (2007).

45. B. C. Buchler, T. Kalkbrenner, C. Hettich, and V. Sandoghdar, Phys. Rev. Lett. **95**, 63003 (2005).

46. S. Ogawa, M. Imada, S. Yoshimoto, M. Okano, and S. Noda, Science. **305**, 227 (2004).

47. P. Lodahl, A. F. van Driel. I. S. Nikolaev, A. Irman, K. Overgaag, D. Vanmaekelbergh, and W. L. Vos, Nature. **430**, 654 (2004).

48. M. Fujita, S. Takahashi, Y. Tanaka, T. Asano, and S. Noda, Science. **308**, 1296 (2005).

49. K. Kounoike, M. Yamaguchi, M. Fujita, T. Asano, J. Nakanishi, and S. Noda, Electron. Lett. **41**, 1402 (2005).

50. Massachusetts Institute of Technology, MIT Photonic-Bands, Web. 4 Nov. 2012, <http://ab-initio.mit.edu/wiki/index.php/MIT_Photonic_Bands>.

51. J. D. Joannopoulos, S. G. Johnson, J. N. Winn, and R. D. Meade, *Photonic Crystals: Molding the Flow of Light*, 2nd edition. (Princeton University, New Jersy, 2008).

52. P. K. Jain, X. Huang, I. H. El-Sayed, and M. A. El-Sayed, Accounts of Chemical Research. **41**, 1578 (2008).

53. A. G. Brolo, S. C. Kwok, M. G. Moffitt, R. Gordon, J. Riordon, and K. L. Kavanagh, J. Am. Chem. Soc. **127**, 42 (2005).

54. J. Song, T. Atay, S. Shi, H. Urabe, and A. V. Nurmikko, Nano Lett. **5**, 1557 (2005).

55. O. Kulakovich, N. Strekal, A. Yaroshevich, S. Maskevich, S. Gaponenko, I. Nabiev, U. Woggon, and M. Artemyev, Nano Lett. **2**, 1449 (2002).

Chapter 3

Theoretical Models of Spontaneous Emission near Planar Structures

In this Chapter we first describe how to apply classical electrodynamics to model spontaneous emission near planar structures. Afterwards, we discuss the quantum theory, with particular emphasis on the relationship between the PDOS and the spontaneous emission rate. We will also show the equivalence between the quantum and the classical models.

3.1 Classical Theory of Dipole Emission near Planar Structures

Classically, we can model spontaneous emission as the result of energy loss due to the radiation of a harmonic dipole oscillator [1]. In particular, as the dipole oscillates, it dissipates energy into radiation modes and its dipole moment decreases. We are interested in calculating the fluorescence lifetime, at which the energy of the dipole decreases to 1 / e of its initial value.

The equation of motion of a harmonically oscillating dipole near a planar interface is [1]:

$$\frac{\mathrm{d}^2}{\mathrm{d}t^2}\langle\langle + \mu^2\langle\langle = \frac{e^2}{m}E_R - b_0\frac{\mathrm{d}}{\mathrm{d}t}\langle\langle , \qquad (3.1.1)$$

where ω is the natural frequency of the dipole in the absence of damping, e is the electron charge, m is the effective mass of the dipole, and t is the time. The reflected electric field at the dipole position due to the presence of planar interfaces is depicted by E_R, while b_0 represents the "intrinsic" fluorescence rate in the absence of any interface. Both of the dipole moment, μ, and E_R oscillate at the same frequency [2]:

$$\mu = \mu_0 e^{-i(\omega+\Delta\omega)t} e^{-bt/2}, \tag{3.1.2}$$

and

$$E_R = E_0 e^{-i(\omega+\Delta\omega)t} e^{-bt/2}, \tag{3.1.3}$$

where μ_0 and E_0 are the dipole moment and electric field amplitude, respectively. We note that optical frequencies are in the range of 10^{15} rad/s, yet fluorescence decay rates are typically of the order of 10^9 s^{-1}. Consequently, it is safe to assume $b_0 << \omega$. Another assumption is that, the interaction with the field E_R is weak such that, $(e^2 / \mu_0\, m)\, E_0 << \omega^2$. Substituting of Eqs. (3.1.2) and (3.1.3) into Eq. (3.1.1), to get [2]:

$$\Delta\omega = \frac{b^2}{8\omega} + \left[\frac{e^2}{2\mu_0 m\omega}\right] \mathrm{Re}(E_0), \tag{3.1.4}$$

and

$$b = b_0 + \left[\frac{e^2}{\mu_0 m\omega}\right] \mathrm{Im}(E_0). \tag{3.1.5}$$

For most cases, the frequency shift is very small [3]. As a result, we will ignore this term in subsequent analysis.

The radiative decay rate, b_r, in a homogeneous medium without the presence of any interface can be given as [1]:

$$b_r = \frac{2}{3}\frac{e^2 k_1^3}{m\omega n_1^2}, \tag{3.1.6}$$

where k_1 is the propagation constant in the medium containing the dipole and n_1 is the refractive index of the same medium. We now define the quantum yield, q, of the dipole as [2]:

$$q = \frac{b_r}{b_0}. \tag{3.1.7}$$

Using Eqs. (3.1.6) and (3.1.7) to simplify Eq. (3.1.5), to find:

$$b = b_0\left[1+\frac{3qn_1^2}{2\varepsilon_0 k_1^3}\mathrm{Im}(E_0)\right]. \tag{3.1.8}$$

Eq. (3.1.8) shows that, the problem now is reduced to the calculation of the reflected field at the dipole position.

Let's consider the problem of two mirrors, shown in Fig. 3.1.1. The dipole is placed in medium 1 and is located at distances d and s from media 2 and 3, respectively. We further assume that the refractive index of any medium is isotropic and can be defined in a general form as:

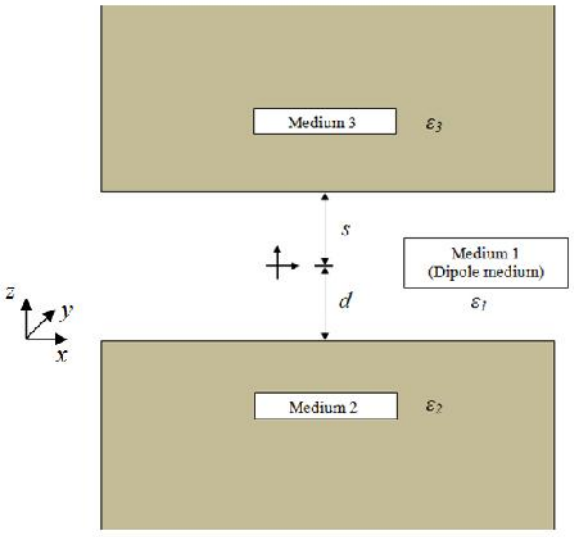

Fig. 3.1.1: Geometry of the two mirrors system. The mirrors are parallel and infinite along the x and y directions.

$$£_j = n_j^2 - K_j^2 + i\,2n_j K_j\,, \tag{3.1.9}$$

where ε_j is the dielectric constant of medium j, while n_j and K_j are the real and imaginary parts of the refractive index of medium j, where j = 1, 2, or 3. The electric field at any point in medium 1, **E**, can be defined as [2]:

$$\mathbf{E} = \frac{1}{£_1}\left[k_1^2\mathbf{\Pi}_1 + \nabla(\nabla\cdot\mathbf{\Pi}_1)\right], \tag{3.1.10}$$

where $\mathbf{\Pi}_1$ is the Hertz vector of medium 1.

Let's consider the first case where the dipole is oriented perpendicular to the interface. Using Sommerfeld theory [4], we can write the Hertz vectors in the three media as (in cylindrical coordinates r, z, ϕ):

$$\mathbf{\Pi}_1 = \hat{e}_z \, « k_1 \int_0^\infty J_0(ur)\frac{u}{l_1}\left[e^{\pm l_1(z-\hat{d})} + f_1 e^{-l_1 z} + f_2 e^{l_1(z-\hat{d}-\hat{s})}\right] du\,, \tag{3.1.11}$$

$$\mathbf{\Pi}_2 = \hat{e}_z \, « k_1 \int_0^\infty f_3 e^{l_2 z} J_0(ur)\frac{u}{l_1} du\,, \tag{3.1.12}$$

and

$$\mathbf{\Pi}_3 = \hat{e}_z \, « k_1 \int_0^\infty f_4 e^{-l_3(z-\hat{d}-\hat{s})} J_0(ur)\frac{u}{l_1} du\,, \tag{3.1.13}$$

where $\hat{d} = k_1 d$, $\hat{s} = k_1 s$, $l_j = -i(\varepsilon_j / \varepsilon_1 - u^2)^{1/2}$. To determine the coefficients f_1, f_2, f_3, and f_4, we apply the boundary conditions at z = 0 [2]:

$$£_1\mathbf{\Pi}_1 = £_2\mathbf{\Pi}_2\,, \tag{3.1.14}$$

$$\frac{\partial\mathbf{\Pi}_1}{\partial z} = \frac{\partial\mathbf{\Pi}_2}{\partial z}\,. \tag{3.1.15}$$

and the boundary conditions at $z = s + d$:

$$£_1\mathbf{\Pi}_1 = £_3\mathbf{\Pi}_3\,, \tag{3.1.16}$$

$$\frac{\partial \mathbf{\Pi}_1}{\partial z} = \frac{\partial \mathbf{\Pi}_3}{\partial z}. \tag{3.1.17}$$

From Eqs. (3.1.14) to (3.1.17), we can find f_1, f_2, f_3, and f_4. Substituting the values of f_1 and f_2, into Eq. (3.1.11) and applying Eq. (3.1.10), we obtain the reflected field at the dipole position and consequently Eq. (3.1.8) can be written as [2]:

$$b_{\perp} = b_0(1 - qZ_{\perp}), \tag{3.1.18}$$

where $b_{\perp}$ is the emitter fluorescence decay rates when the dipole is perpendicular to the interfaces. The parameter $Z_{\perp}$ summarizes the impact of the planar interface on the dipole fluorescence decay rate when it is perpendicular to the interfaces, and it is defined as [2]:

$$Z_{\perp} = 1 - \frac{3}{2}\,\mathrm{Im}\int_0^{\infty} du\,\frac{u^3}{l_1}\left[\frac{F(\hat{d}, -R_{12}^{//})F(\hat{s}, -R_{13}^{//})}{F(\hat{d}+\hat{s}, -R_{12}^{//}R_{13}^{//})}\right], \tag{3.1.19}$$

where $F(x, y) = 1 + y\exp(-2l_1x)$, while $R_{12}^{//}$ and $R_{13}^{//}$ refer to the reflection coefficients at the medium 1 / medium 2 and medium 1 / medium 3 interfaces for p-polarization, respectively. These reflection coefficients are defined as [2]:

$$R_{ab}^{//} = \frac{£_a l_b - £_b l_a}{£_a l_b + £_b l_a}. \tag{3.1.20}$$

Consider now the second case where the dipole is oriented parallel to the interfaces. In this case, the Hertz vectors can be written as:

$$\mathbf{\Pi}_1 = \hat{e}_x \, k_1 \int_0^{\infty} J_0(ur)\frac{u}{l_1}\left[e^{\pm l_1(z-\hat{d})} + f_1 e^{-l_1 z} + f_2 e^{l_1(z-\hat{d}-\hat{s})}\right] du$$

$$+\hat{e}_z \, k_1 \frac{x}{r}\left[\int_0^{\infty} g_1 e^{-l_1 z} J_1(ur)du + \int_0^{\infty} g_2 e^{l_1(z-\hat{d}-\hat{s})} J_1(ur)du\right], \tag{3.1.21}$$

$$\mathbf{\Pi}_2 = \hat{e}_x \, k_1 \int_0^{\infty} f_3 e^{l_2 z} J_0(ur)\frac{u}{l_1}du + \hat{e}_z \, k_1 \frac{x}{r}\int_0^{\infty} g_3 e^{l_2 z} J_1(ur)du, \tag{3.1.22}$$

and

$$\mathbf{\Pi}_3 = \hat{e}_x \, k_1 \int_0^\infty f_4 e^{-l_3(z-\hat{d}-\hat{s})} J_0(ur) \frac{u}{l_1} du + \hat{e}_z \, k_1 \frac{x}{r} \int_0^\infty g_3 e^{-l_3(z-\hat{d}-\hat{s})} J_1(ur) du \,, \quad (3.1.23)$$

The boundary conditions at $z = 0$ are:

$$\frac{\partial \mathbf{\Pi}_{1z}}{\partial z} - \frac{\partial \mathbf{\Pi}_{2z}}{\partial z} = \frac{\partial \mathbf{\Pi}_{2x}}{\partial x} - \frac{\partial \mathbf{\Pi}_{1x}}{\partial x}, \quad (3.1.24)$$

$$£_1 \frac{\partial \mathbf{\Pi}_{1x}}{\partial z} = £_2 \frac{\partial \mathbf{\Pi}_{2x}}{\partial z}, \quad (3.1.25)$$

$$£_1 \mathbf{\Pi}_{1x} = £_2 \mathbf{\Pi}_{2x} \,, \quad (3.1.26)$$

and

$$£_1 \mathbf{\Pi}_{1z} = £_2 \mathbf{\Pi}_{2z} \,. \quad (3.1.27)$$

The boundary conditions at $z = s + d$ are similar to the previous conditions but only with replacing parameters associated with medium 3 with those of medium 2. By applying the boundary conditions, and using Eqs. (3.1.8), (3.1.10), and (3.1.11), we get [2]:

$$b_{//} = b_0 (1 - q Z_{//}) \,, \quad (3.1.28)$$

Where $b_{//}$ is the emitter fluorescence decay rate when the dipole is parallel to the interfaces. The parameter $Z_{//}$ is given by [2]:

$$Z_{//} = 1 - \frac{3}{4} \int_0^\infty du \, \frac{u}{l_1} \left[\frac{F(\hat{d}, R_{12}^{\perp}) F(\hat{s}, R_{13}^{\perp})}{F(\hat{d}+\hat{s}, -R_{12}^{\perp} R_{13}^{\perp})} + \left(1 - \frac{u^2}{l_1^2}\right) \frac{F(\hat{d}, R_{12}^{//}) F(\hat{s}, R_{13}^{//})}{F(\hat{d}+\hat{s}, -R_{12}^{//} R_{13}^{//})} \right], \quad (3.1.29)$$

where $R_{12}^{\perp}$ and $R_{13}^{\perp}$ refer to the reflection coefficients at the medium 1 / medium 2 and medium 1 / medium 3 interfaces for s-polarization. These reflection coefficients are defined as:

$$R_{ab}^{\perp} = \frac{l_a - l_b}{l_a + l_b} \,. \quad (3.1.30)$$

The fluorescence lifetime of the dipole, τ, is defined as the inverse of the fluorescence decay rate. Using Eqs. (3.1.18) and (3.1.28), the lifetime can be represented as:

$$^{2}_{\perp,//} = \frac{^{2}_{0}}{(1-qZ_{\perp,//}}, \tag{3.1.31}$$

where τ_0 ($\equiv 1 / b_0$) is the intrinsic fluorescence lifetime of the dipole in the absence of any interface.

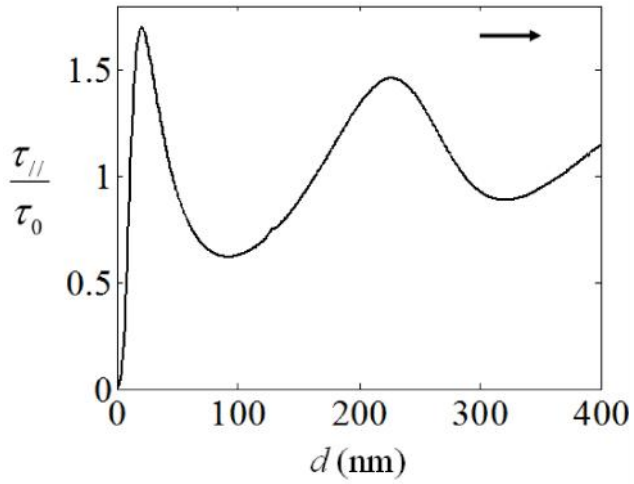

Fig. 3.1.2: Change of the normalized fluorescence lifetime versus distance for (silver / fluorophore on the top of fatty acid film / air) double mirror system when the dipole is parallel to the interfaces.

Fig. 3.1.2 shows the change of the normalized fluorescence lifetime, $^{2}_{//} / \tau_0$, with the distance, d, for (silver / fluorophore on the top of fatty acid film / air). In this figure, it is assumed that the emission wavelength = 612 nm, q = 0.85, s = 0, and the dipole is parallel to the interfaces. Similarly, Fig. 3.1.3 shows the change of $^{2}_{\perp} / \tau_0$ for (silicon / fluorophore on the top of fatty acid film / air) such that the emission wavelength = 621 nm, q = 0.85, s = 0, and the dipole is perpendicular to the interfaces.

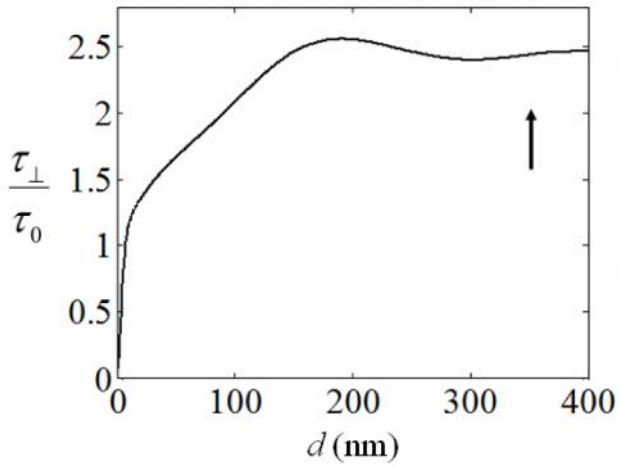

Fig. 3.1.3: Change of the normalized fluorescence lifetime versus distance for (silicon / fluorophore on the top of fatty acid film / air) double mirror system when the dipole is perpendicular to the interfaces.

3.2 Equivalence of the Quantum and the Classical Models

In this section we use the quantum theory to calculate the spontaneous emission, radiative, rate of a two-level quantum system located at **r** = $\mathbf{r}_0$. Fig. 3.2.1 illustrates our problem which considers a transition from the excited state $|i\rangle$ with energy E_i to a set of final states $|f\rangle$ with identical energy E_f but they are only different in the mode of radiation field **k**. To avoid confusion, **k** is not the wavevector, however, it just denotes a specific mode characterized by the wavevector and the polarization vector.

The Fermi's Golden rule defines the spontaneous emission rate b_r as [5]:

$$b_r = \frac{2\pi}{\hbar^2}\sum_f |\langle f|\hat{H}_I|i\rangle|^2 \delta(\omega_i - \omega_f), \qquad (3.2.1)$$

where $\hat{H}_I$ is the interaction Hamiltonian in the dipole approximation and defined as [5]:

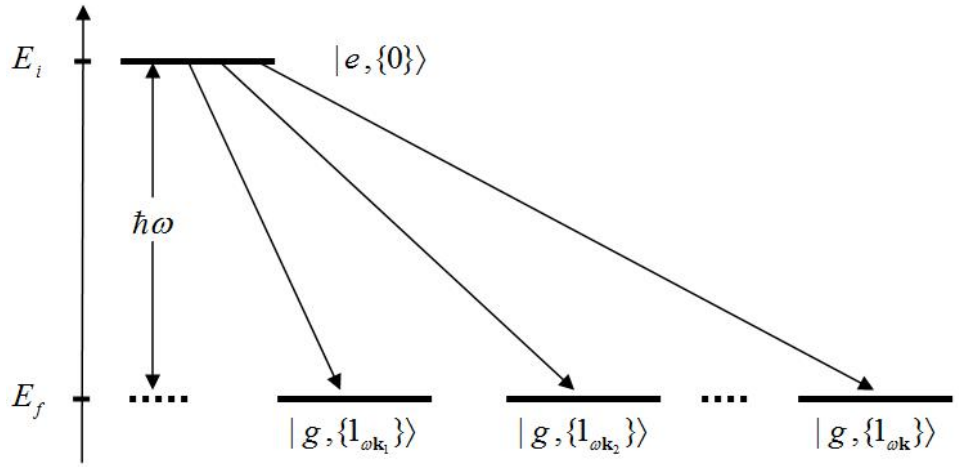

Fig. 3.2.1: Transition from an initial state $|i\rangle$ to a set of final states $|f\rangle$.

$$\hat{H}_{\mathrm{I}} = -\hat{\boldsymbol{\mu}}\cdot\hat{\mathbf{E}}. \tag{3.2.2}$$

Using Eq. (3.2.2), we can substitute as follows:

$$|\langle f|\hat{H}_{\mathrm{I}}|i\rangle|^2 = \langle i|\hat{\boldsymbol{\mu}}\cdot\hat{\mathbf{E}}|f\rangle\langle f|\hat{\boldsymbol{\mu}}\cdot\hat{\mathbf{E}}|i\rangle. \tag{3.2.3}$$

The electric field operator, $\hat{\mathbf{E}}$, at $\mathbf{r} = \mathbf{r}_0$ can be represented as [6]:

$$\hat{\mathbf{E}} = \sum_{\mathbf{k}}\left[\mathbf{E}_{\mathbf{k}}^{+}\hat{a}_{\mathbf{k}}(t) + \mathbf{E}_{\mathbf{k}}^{-}\hat{a}_{\mathbf{k}}^{\dagger}(t)\right], \tag{3.2.4}$$

where $\mathbf{E}_{\mathbf{k}}^{+}$ and $\mathbf{E}_{\mathbf{k}}^{-}$ are the positive and negative frequency parts of the complex electric field $\mathbf{E}_{\mathrm{k}}$ of mode $\mathbf{k}$, respectively. While, $\hat{a}_{\mathbf{k}}(t)$ and $\hat{a}_{\mathbf{k}}^{\dagger}(t)$ are defined as [6]:

$$\hat{a}_{\mathbf{k}}(t) = \hat{a}_{\mathbf{k}}(0)\exp(-i\mu_{\mathbf{k}}t), \qquad \hat{a}_{\mathbf{k}}^{\dagger}(t) = \hat{a}_{\mathbf{k}}^{\dagger}(0)\exp(-i\mu_{\mathbf{k}}t), \tag{3.2.5}$$

where $\hat{a}_{\mathbf{k}}(0)$ and $\hat{a}_{\mathbf{k}}^{\dagger}(0)$ are the annihilation and creation operators, respectively. The dipole moment operator « can be written as [5]:

$$\hat{\alpha} = \alpha\left[\hat{r}^{+} + \hat{r}\right], \text{ with } \hat{r}^{+} = |e\rangle\langle g| \text{ and } \hat{r} = |g\rangle\langle e|. \tag{3.2.6}$$

Using Eqs. (3.2.4), (3.2.5), and (3.2.6), to get:

$$\hat{\alpha}\cdot\hat{\mathbf{E}} = \sum_{\mathbf{k}} \hat{\alpha}\cdot\left[\mathbf{E}_{\mathbf{k}}^{+}\hat{r}^{+}\hat{a}_{\mathbf{k}}(t) + \mathbf{E}_{\mathbf{k}}^{-}\hat{r}\,\hat{a}_{\mathbf{k}}^{\dagger}(t) + \mathbf{E}_{\mathbf{k}}^{+}\hat{r}\,\hat{a}_{\mathbf{k}}(t) + \mathbf{E}_{\mathbf{k}}^{-}\hat{r}^{+}\hat{a}_{\mathbf{k}}^{\dagger}(t)\right]. \tag{3.2.7}$$

The initial and final states of the system (field + atom) can be given as:

$$|i\rangle = |e,\{0\}\rangle = |e\rangle|\{0\}\rangle, \tag{3.2.8}$$

$$|f\rangle = |g,\{1_{\mu_{\mathbf{k}'}}\}\rangle = |g\rangle|\{1_{\mu_{\mathbf{k}'}}\}\rangle, \tag{3.2.9}$$

where $|\{0\}\rangle$ is the zero-photon state, and $|\{1_{\mu_{\mathbf{k}'}}\}\rangle$ is the one-photon state associated with mode **k**'. Operating with $\hat{\boldsymbol{\mu}}\cdot\hat{\mathbf{E}}$ on the state $|i\rangle$, to find [5]:

$$\hat{\boldsymbol{\mu}}\cdot\hat{\mathbf{E}}|i\rangle = \boldsymbol{\mu}\cdot\sum_{\mathbf{k}}\mathbf{E}_{\mathbf{k}}^{-}e^{i\mu_{\mathbf{k}}t}|g,\{1_{\mu_{\mathbf{k}'}}\}\rangle. \tag{3.2.10}$$

Operating with $|f\rangle$ on Eq. (3.2.10), to give [5]:

$$|f\rangle\hat{\boldsymbol{\mu}}\cdot\hat{\mathbf{E}}|i\rangle = \boldsymbol{\mu}\cdot\sum_{\mathbf{k}}\mathbf{E}_{\mathbf{k}}^{-}e^{i\mu_{\mathbf{k}}t}|g,\{1_{\mu_{\mathbf{k}'}}\}|g,\{1_{\mu_{\mathbf{k}}}\}\rangle. \tag{3.2.11}$$

Using a similar procedure leads us to [5]:

$$|i\rangle\hat{\boldsymbol{\mu}}\cdot\hat{\mathbf{E}}|f\rangle = \boldsymbol{\mu}\cdot\sum_{\mathbf{k}}\mathbf{E}_{\mathbf{k}}^{+}e^{-i\mu_{\mathbf{k}}t}|g,\{1_{\mu_{\mathbf{k}}}\}|g,\{1_{\mu_{\mathbf{k}'}}\}\rangle. \tag{3.2.12}$$

Substituting of Eqs. (3.2.11) and (3.2.12) into Eq. (3.2.3) and using the result in Eq. (3.2.1), to find:

$$b_r = \frac{2\pi}{\hbar^2}\sum_{\mathbf{k}}\sum_{\mathbf{k}''}\left[\boldsymbol{\mu}\cdot\mathbf{E}_{\mathbf{k}''}^{+}\mathbf{E}_{\mathbf{k}}^{-}\cdot\boldsymbol{\mu}\right]e^{i(\mu_{\mathbf{k}}-\mu_{\mathbf{k}''})t}$$

$$\times\sum_{\mathbf{k}'}\langle g,\{1_{\mu_{\mathbf{k}''}}\}|g,\{1_{\mu_{\mathbf{k}'}}\}\rangle\langle g,\{1_{\mu_{\mathbf{k}'}}\}|g,\{1_{\mu_{\mathbf{k}}}\}\rangle\delta(\mu_{\mathbf{k}'}-\mu). \tag{3.2.13}$$

Due to the orthogonality, all terms vanish except those for which **k'** = **k''** = **k**. therefore, Eq. (3.2.13) can be written as:

$$b_r = \frac{2\pi}{\hbar^2}\sum_{\mathbf{k}}\left[\boldsymbol{\mu}\cdot\mathbf{E}_{\mathbf{k}}^{+}\mathbf{E}_{\mathbf{k}}^{-}\cdot\boldsymbol{\mu}\right]\delta(\omega_{\mathbf{k}}-\omega). \tag{3.2.14}$$

It is convenient to rewrite $\mathbf{E}_{\mathbf{k}}^{+}$ and $\mathbf{E}_{\mathbf{k}}^{-}$ as [5]:

$$\mathbf{E}_{\mathbf{k}}^{+} = \sqrt{\frac{\hbar\omega_{\mathbf{k}}}{2\varepsilon_0}}\mathbf{u}_{\mathbf{k}} \quad \text{and} \quad \mathbf{E}_{\mathbf{k}}^{-} = \sqrt{\frac{\hbar\omega_{\mathbf{k}}}{2\varepsilon_0}}\mathbf{u}_{\mathbf{k}}^{*}, \tag{3.2.15}$$

where $\mathbf{u}_{\mathbf{k}}$ are normal modes. Since the delta function imposes $\omega_k = \omega$, Eq. (3.2.14) can be written as [5]:

$$b_r = \frac{2\pi}{3\hbar\varepsilon_0}|\boldsymbol{\mu}|^2\,\rho(\mathbf{r}_0,\omega), \tag{3.2.16}$$

where $\rho(\mathbf{r}_0,\omega)$ is the PDOS defined as [5]:

$$\rho(\mathbf{r}_0,\omega) = 3\sum_{\mathbf{k}}\left[\mathbf{n}_{\alpha}\cdot(\mathbf{u}_{\alpha}\mathbf{u}_{\alpha}^{*})\cdot\mathbf{n}_{\alpha}\right]\delta(\omega_{\mathbf{k}}-\omega), \tag{3.2.17}$$

where $\mathbf{n}_{\mu}$ is a unit vector in the direction of $\boldsymbol{\mu}$. It is more convenient to represent $\rho(\mathbf{r}_0,\omega)$ in terms of the dyadic Green's function instead of normal modes, such that [5]:

$$\rho(\mathbf{r}_0,\omega) = \frac{6\pi\omega}{\pi c^2}\left[\mathbf{n}_{\alpha}\cdot\mathrm{Im}\left\{\overleftrightarrow{\mathbf{G}}(\mathbf{r}_0,\mathbf{r}_0;\omega)\right\}\cdot\mathbf{n}_{\alpha}\right]. \tag{3.2.18}$$

In an inhomogeneous medium, the dyadic Green's function can be divided into a homogeneous part $\overleftrightarrow{\mathbf{G}}_0$ and a reflection part $\overleftrightarrow{\mathbf{G}}_{\mathrm{ref}}$ at the dipole position, such that:

$$\overleftrightarrow{\mathbf{G}}(\mathbf{r}_0,\mathbf{r}_0;\omega) = \overleftrightarrow{\mathbf{G}}_0(\mathbf{r}_0,\mathbf{r}_0;\omega) + \overleftrightarrow{\mathbf{G}}_{\mathrm{ref}}(\mathbf{r}_0,\mathbf{r}_0;\omega). \tag{3.2.19}$$

Using the definition that the fluorescence decay rate is the sum of the radiative and nonradiative decay rates, *b* can be written as:

$$b = b_0 \left\{ 1 - q \left[1 - \frac{\circ_s(\mathbf{r}_0, \mu)}{\circ_0(\mathbf{r}_0, \mu)} \right] \right\}, \tag{3.2.20}$$

where $\rho_s(\mathbf{r}_0,\omega)$ and $\rho_0(\mathbf{r}_0,\omega)$ are the PDOS in inhomogeneous and homogeneous media respectively. Substituting of Eqs. (3.2.18) and (3.2.19) into Eq. (3.2.20), to get:

$$b = b_0 \left\{ 1 + q \left[\frac{\mathbf{n}_{\ll} \cdot \mathrm{Im}\left\{ \overleftrightarrow{\mathbf{G}}_{\mathrm{ref}}(\mathbf{r_0}, \mathbf{r_0}; \mu) \right\} \cdot \mathbf{n}_{\ll}}{\mathbf{n}_{\ll} \cdot \mathrm{Im}\left\{ \overleftrightarrow{\mathbf{G}}_0(\mathbf{r_0}, \mathbf{r_0}; \mu) \right\} \cdot \mathbf{n}_{\ll}} \right] \right\}. \tag{3.2.21}$$

The reflected electric field at the dipole position, $\mathbf{E}_R$, is related to the dyadic Green's functions as [5]:

$$\mathbf{E}_R = \frac{\mu^2}{£_0 c^2} \overleftrightarrow{\mathbf{G}}_{ref}(\mathbf{r_0}, \mathbf{r_0}; \mu) \boldsymbol{\mu}, \tag{3.2.22}$$

where ε_0 is the free space permittivity and c is the speed of light. The homogeneous part of the dyadic Green's function is given by [5]:

$$\mathbf{n}_{\ll} \cdot \mathrm{Im}\left\{ \overleftrightarrow{\mathbf{G}}_0(\mathbf{r_0}, \mathbf{r_0}; \mu) \right\} \cdot \mathbf{n}_{\ll} = 4®£_0 . \frac{n_1 \mu}{6® c}, \tag{3.2.23}$$

Substituting of Eqs. (3.2.22) and (3.2.23) into Eq. (3.2.21) proves that Eq. (3.2.21) is consistent with the classical derivation (Eq. 3.1.8).

References

1. H. Kuhn, J. Chem. Phys. **53**, 101 (1970).
2. R. R. Chance, A. Prock, and R. Silbey, Adv. Chem. Phys. **37**, 1 (1978).
3. R. R. Chance, A. Prock, and R. Silbey, Phys. Rev. **A12**, 1448 (1975).
4. A. Sommerfeld, *Partial Differential Equations of Physics*, 2nd edition, (Academic, New York, 1949).
5. L. Novotny, B. Hecht, *Principles of Nano-Optics*, 1st edition, (Cambridge University, New York, 2006).
6. R. Loudin, *the Quantum Theory of Light*, 2nd edition, (Oxford University, New York, 1983).

Chapter 4

Probing the Photonic Density of States using Layer-by-Layer Self-Assembly

4.1 Introduction

It is well known that an optical micro- or nano-structure can have a dramatic impact on the process of spontaneous emission in its vicinity. For example, significant enhancement or inhibition of spontaneous emission can be realized using structures such as photonic crystals [1, 2], high Q cavities [3], plasmonic nanostructures [4, 5], dielectric random media [6], and metamaterials [7]. By taking advantage of the Purcell effect [8], it is also possible to engineer spontaneous emission to realize devices such as single photon sources [9] and thresholdless lasers [10].

A fluorophore's spontaneous emission rate is controlled by vacuum field fluctuations and is proportional to the PDOS [11, 12]. To characterize the modified PDOS, one can vary the distance between a fluorophore and underlying optical structures and monitor the changes in fluorescence dynamics. Previously, this distance has been controlled with methods such as Langmuir-Blodgett films [13], thermal evaporation of a dielectric thin film [14], near-field scanning [15], or LbL assembly [16]. In this Chapter, we use LbL assembly to control the distance between the fluorophores and a planar substrate and

correlate the resultant change in fluorescence dynamics with the predicted PDOS. Compared to other methods of distance control, the LbL approach has the important advantage of being capable of generating conformal films with sub-nm thickness control [17] on almost any surface with relative ease. Therefore, this method can be applied to a large variety of optical micro- and nanostructures. Post-fabrication tuning of film thickness is also possible [18]. Unlike [16], here we demonstrate that fluorophores self-assembled on LbL films can be used to experimentally quantify the modification of PDOS. Using discrete emitters and additional nanolithography [17], it is also possible to investigate 3D PDOS modifications.

4.2 Samples Fabrication

The fluorescent samples were fabricated using the self-assembly approach reviewed in Chapter 2. In this experiment, we used two different types of fluorophores, fluorescent nanospheres and colloidal QDs, and two different substrates: planar gold films and silicon wafers. In total, we considered four different types of samples: fluorescent nanospheres on gold, fluorescent nanospheres on silicon, QDs on gold, and QDs on silicon.

Gold substrates were fabricated using electron beam evaporation as illustrated in Fig. (4.2.1). First, we put titanium in a form of ingots inside a crucible. This crucible was cooled by water circulation inside the chamber of the electron beam evaporator. Afterwards, we used a vacuum pump to reduce the pressure within the chamber of the electron beam evaporator to $\sim 10^{-5}$ Torr. In order to melt the ingots, we used electron beams focused on the ingot and accelerated them to a high kinetic energy using a voltage

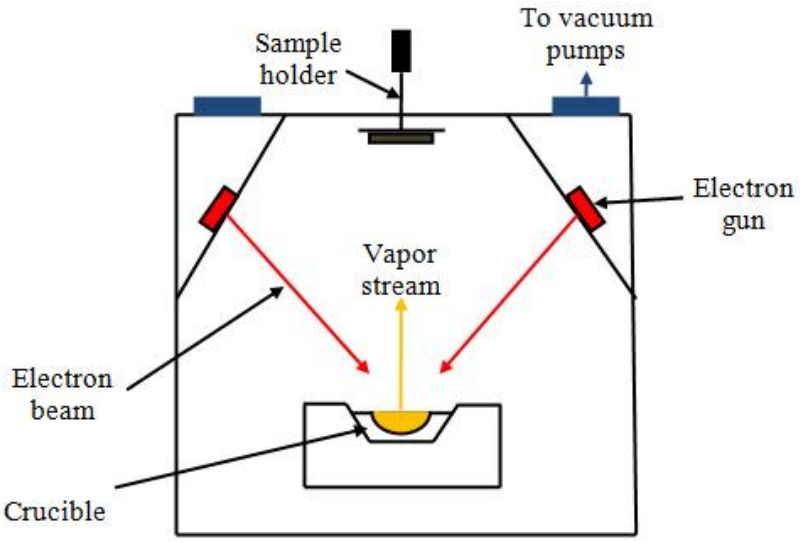

Figure 4.2.1: Schematic of electron beam evaporator.

between 20 kV–25 kV. As we increased the beamcurrent to 80–100 mA, the titanium was evaporated and deposited onto sample surface. We used this technique to deposit 10 nm film of titanium on glass substrates. The titanium film served as an adhesion layer under gold to enhance its mechanical properties and to avoid damaging it during sonication. After titanium film deposition, we then used similar method to deposit 100 nm of gold on the titanium layer.

The procedure of forming LbL film on gold is shown schematically in Fig. (4.2.2). In this case, the assembly process was carried out by first immersing the gold coated glass slide in a thiol solution (16-mercapto-hexadecanoic acid (MHDA), 1 mM, pH ~ 2) for 24 hours, followed by ethanol sonication and DI water rinsing. During this step, a monolayer of ω-COOH thiol was adsorbed onto the gold film to form a negatively charged layer.

Afterwards, we immersed the negatively charged sample in a cationic solution of PAH (2

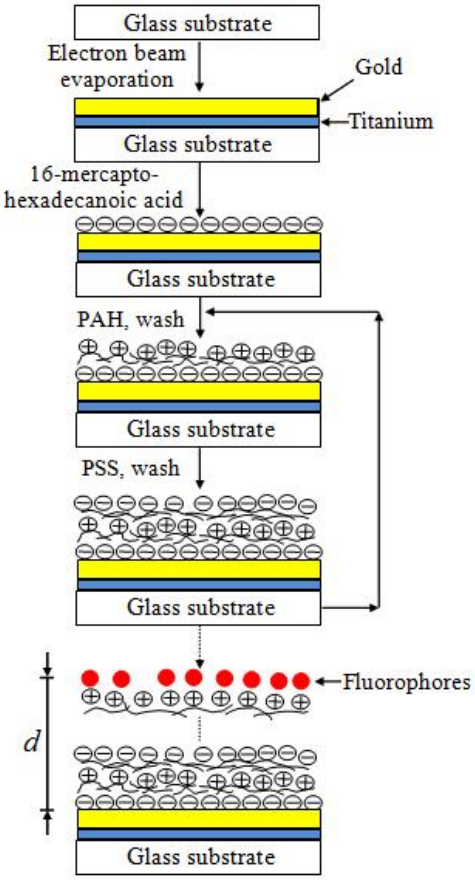

Fig. 4.2.2: Schematic of the LbL self-assembly on a gold substrate.

mg/ml, pH ~ 7). Due to electrostatic interaction, a positively charged PAH monolayer was deposited over the thiol group. Then, after rinsing in DI water, we immersed the sample in an anionic solution of PSS (3 mg/ml, pH ~ 7) to deposit a negatively charged PSS monolayer over PAH. This deposition process can be repeated many times to form any desired number of PAH/PSS bilayer films over the gold substrate. After obtaining the desired number of layers, ending with a positively charged PAH layer, we immersed the sample in an aqueous suspension of negatively charged fluorophores which then adsorbed onto the film surface.

The two types of fluorophores we used in this study are fluorescent polystyrene

nanospheres (purchased from Phosphorex, emission peak at 680 nm, 27 nm mean diameter) with negatively charged carboxyl functionalization, and colloidal CdSe/ZnS core/shell QDs (from NN-LABS, emission peak at 621 nm, 5 nm mean diameter) coated with negatively charged mercaptoundecanoic acid ligands. Typical distributions of fluorescent nanospheres and QDs over gold substrate were obtained using AFM. Two representative examples are shown in Figs. (4.2.3) and (4.2.4), respectively.

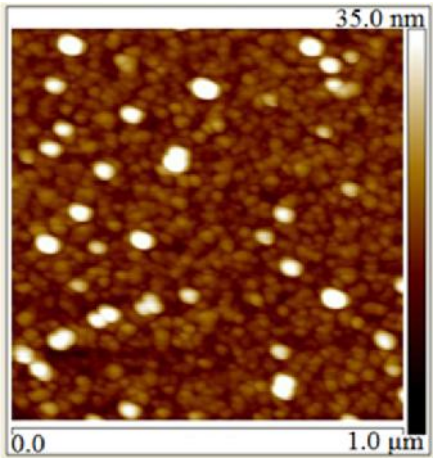

Figure 4.2.3: AFM images of fluorescent nanospheres assembled above gold.

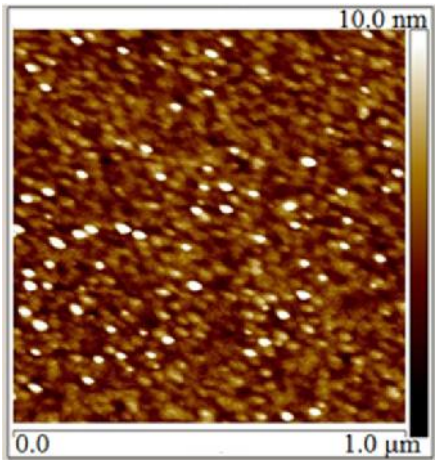

Fig. 4.2.4: AFM images of QDs assembled above gold.

A schematic representation of depositing LbL film on silicon wafers is shown in Fig. (4.2.5). These wafers were prepared by RCA cleaning process [19] which involved a 20 minutes bath at 70 ^{o}C in a $NH_4OH–H_2O_2–H_2O$ (5:1:1 v/v) cationic solution to remove any organic contamination from the Si surfaces. During this step, a very thin layer of silicon dioxide (SiO_2) was formed on the Si surface and the OH^- ions of the cationic solution were bounded to the SiO_2 layer to form an anionic layer that initiated LbL self–assembly deposition. Afterwards, the substrates were cleaned from any metallic contaminations in $HCl–H_2O_2–H_2O$ (6:1:1 v/v) at 70 ^{o}C for 5 minutes. The Si wafers were rinsed thoroughly in DI water for 2 minutes after each bath. The wafers were then immersed for 3 minutes in a cationic aqueous solution of dissolved PAH (2 mg/ml, pH ~ 7).

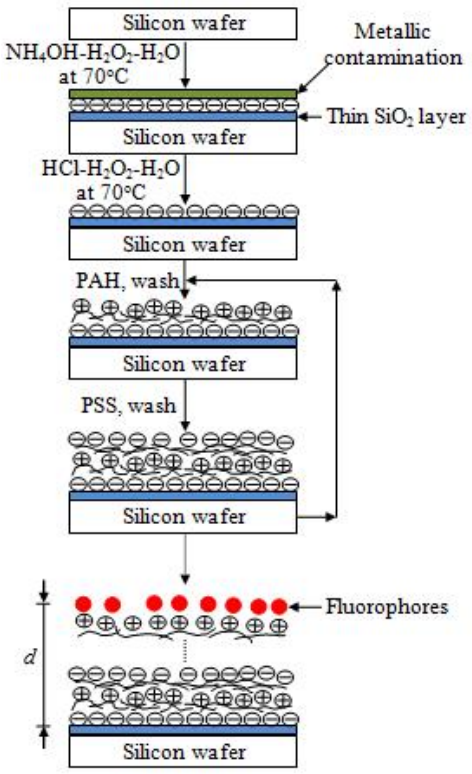

Figure 4.2.5: Schematic of the LbL self-assembly on a silicon wafer.

Again the wafers were rinsed in DI water for 2 minutes and then immersed for 3 minutes in an anionic aqueous solution of dissolved Poly PSS (3 mg/ml, pH ~ 7), followed by a wash in DI water for 2 minutes. The outermost layer of the deposited LbL films was always selected to be PAH. By sequential adsorption of PAH and PSS, the thickness of the film on each silicon wafer could be controlled with nanoscale accuracy by changing the number of PAH/PSS bilayers.

Ellipsometry measurements yielded a film refractive index of 1.45 and a thickness of 3 nm per bilayer. After obtaining the desired number of layers, we immersed the sample in an aqueous suspension of the negatively charged fluorophores which then adsorbed onto the film surface.

The distributions of fluorescent nanospheres and QDs assembled over silicon substrate, imaged by AFM, are shown in Figs. (4.2.6) and (4.2.7), respectively. As can be observed, the fluorophores are dispersed separately without any aggregation.

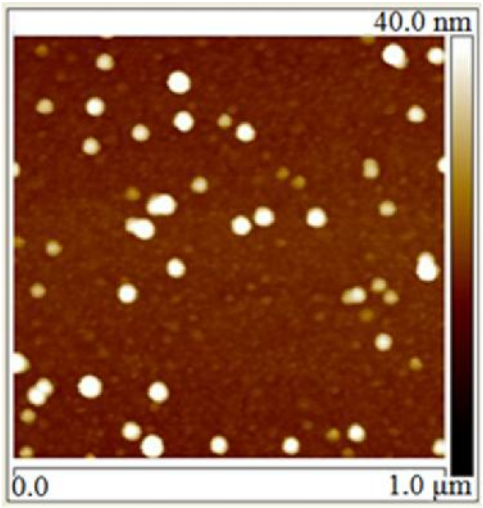

Figure 4.2.6: AFM images of fluorescent nanospheres assembled above silicon.

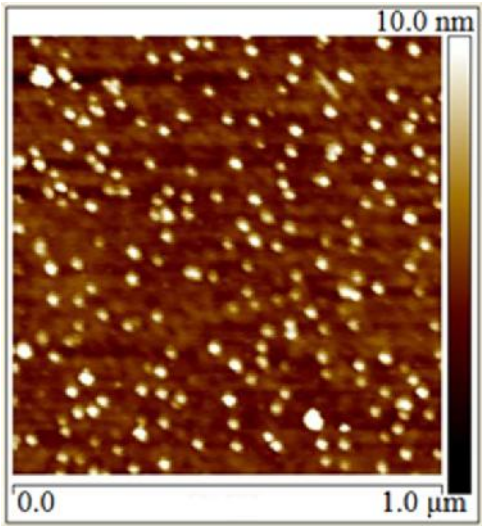

Figure 4.2.7: AFM images of QDs assembled above silicon.

4.3 Fluorescence Lifetime Measurements

The experimental setup used for fluorescence lifetime measurement is shown schematically in Fig. (4.3.1). In this setup, the fluorophores are excited using a picoseconds diode laser (model BDL-473-C from Becker and Hickl). This source produces blue light of 473 nm wavelength, 40 ps pulse width, 20 MHz repetition rate, and 0.7 mm beam diameter. The emitted light from the laser diode is reflected using a mirror in a direction of longpass dichroic filter (LPDF) (model DMLP425 from Thorlabs), which is used to selectively pass red light, emitted from fluorophores, and reflect the blue light of the diode laser. Specifically, the LPDF has a greater than 90% average reflectivity in the 380-490 nm band and a greater than 90% transmissivity in the 520-700 nm band. This LPDF directs the blue laser beam to an objective lens (model M Plan APO 50X from Mitutoyo) that focuses the laser light beam on the sample surface to a beam of around 3 µm diameter. This focused light excites the fluorophores assembled over gold or

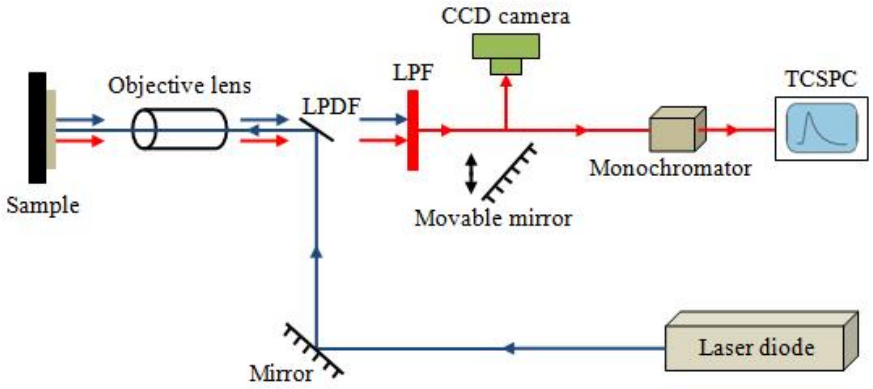

Figure 4.3.1: Schematic of the experimental setup for spontaneous emission lifetime measurements.

silicon to generate fluorescent signals. The sample surface reflects both the blue pump light and red fluorescent signal. The LPDF allows the fluorescent signal to pass through and remove the most of the pump light. Subsequently, we use an optical longpass filter to remove the remaining pump light. In order to image the fluorescent signal, as shown in Fig. (4.3.2), we can use a movable mirror to reflect the fluorescent red light in a direction of a charge-coupled device (CCD) camera (model DFK 21B404 from ImagingSource). Otherwise, the light is directed toward a monochromator (model H10/1200 from Horiba Jobin Yvon) to select the wavelength that corresponds to the maximum fluorescent intensity. Finally, the photoluminescence from the used fluorophores is detected by the single photon counter and its lifetime is recorded using TCSPC (Picoharp 300 from PicoQuant).

In this setup, the axis of the photon counter is perpendicular to the sample surface. As a result, we can assume that the detected photons are emitted from the dipoles which are parallel to the interfaces in the LbL film. This is because the dipoles perpendicular to the interfaces emit photons in a direction perpendicular to the axis of the photon counter.

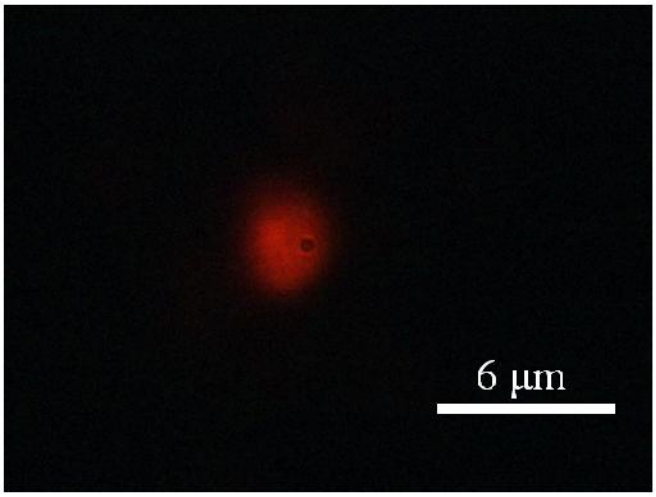

Figure 4.3.2: Fluorescent image captured by the CCD camera of QDs assembled over gold.

4.4 Results and Discussions

We experimentally investigated four different combinations of fluorophores (nanospheres and QDs) and planar substrates (gold and silicon). As illustrated in Figs. (4.2.2) and (4.2.5), the parameter *d* refers to the distance between the center of the fluorophore and the planar substrate. Representative examples, at different values of *d*, of fluorescence decay of the fluorescent nanospheres assembled over gold and silicon substrates are shown in Figs. (4.4.1) and (4.4.2), respectively. Similarly, Figs. (4.4.3) and (4.4.4) illustrate examples, at different values of *d*, of fluorescence decay of the QDs assembled over gold and silicon substrates, respectively.

Figs. (4.4.1) and (4.4.2) show that photoluminescence decay of the fluorescent nanospheres is single exponential and can be easily extracted through exponential fitting. However, the fluorescence dynamics of the QDs, which are shown in Figs. (4.4.3) and (4.4.4), are multi-exponential and cannot be easily fitted using a single exponential

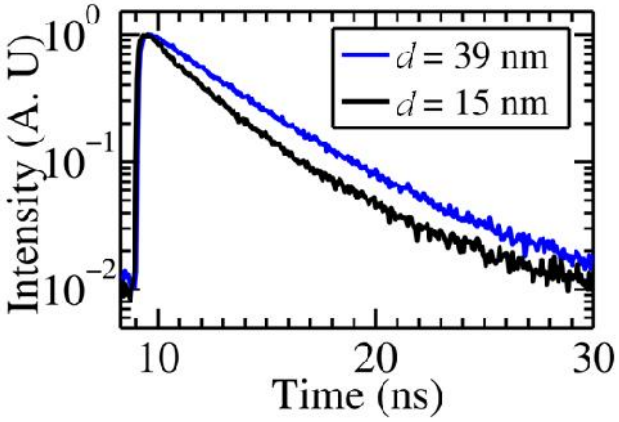

Figure 4.4.1: Fluorescence decay in fluorescent nanospheres assembled above gold.

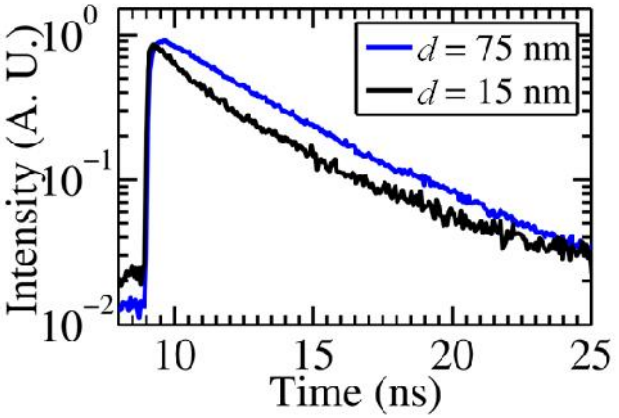

Figure 4.4.2: Fluorescence decay in fluorescent nanospheres assembled above silicon.

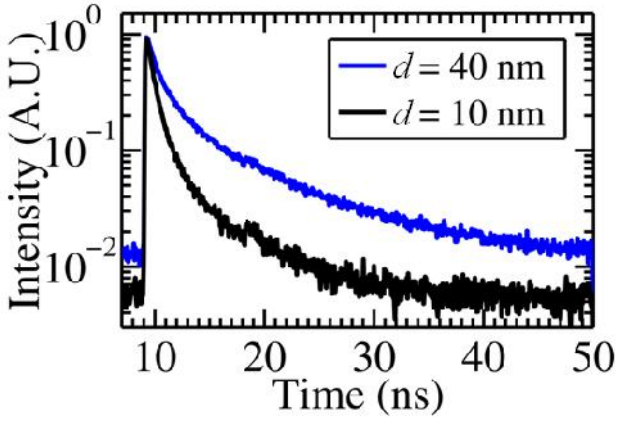

Figure 4.4.3: Fluorescence decay in QDs assembled above gold.

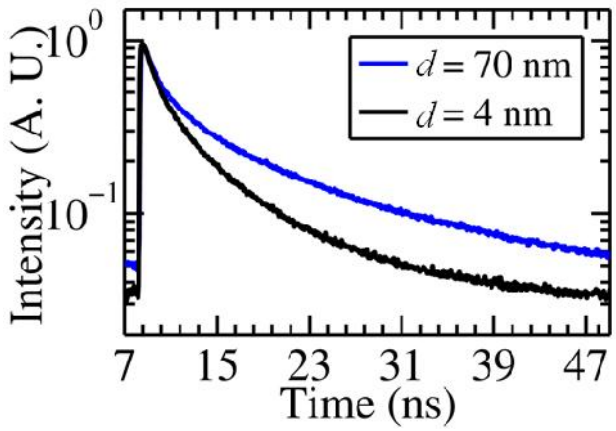

Figure 4.4.4: Fluorescence decay in QDs assembled above silicon.

function. One possible explanation for this phenomenon is QD blinking due to charge trapping [20].

To facilitate quantitative analysis, we define an average fluorescence lifetime τ as [21]:

$$\tau = \frac{\int_0^\infty t\, I(t)\, dt}{\int_0^\infty I(t)\, dt}, \tag{4.2.1}$$

where $I(t)$ represents the experimentally obtained photoluminescence intensity.

Figs. (4.4.5) and (4.4.6) compare the theoretical fluorescence lifetime with experimental data for using fluorescent nanospheres and QDs, respectively. Experimental values of τ were extracted from $I(t)$ using Eq. (4.2.1). Its standard deviation was calculated from measurements at 8 distinct locations on the same sample. For comparison with theory, we choose q and τ_0 as fitting parameters in Eq. (3.1.31) while Z was calculated from Eq. (3.1.29) using gold and silicon dielectric functions from Refs. [22,23]. To account for finite nanosphere size, we assume that the fluorophores are uniformly distributed within the nanosphere with radius r and located at the origin (i.e., at z = 0). The area of a cross section of the sphere at height z divided by the volume of the sphere is:

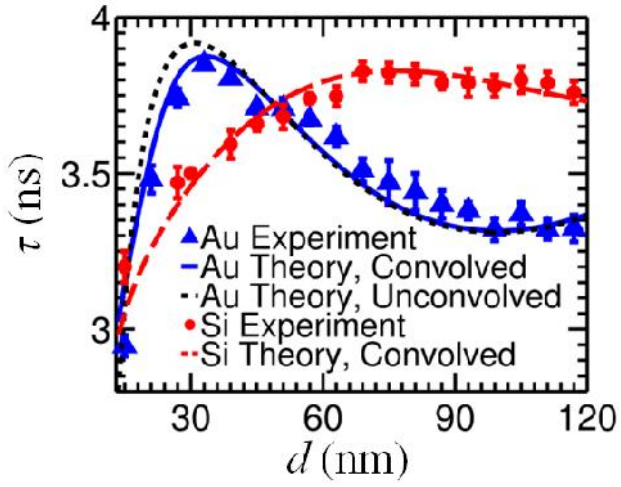

Figure 4.4.5: Theoretical and experimental values of fluorescence lifetime as a function of the distance *d* for fluorescent nanospheres. For nanospheres on Au, both convolved (solid blue line) and unconvolved (dashed black line) theoretical results are shown. Only convolved theory is shown for nanospheres on Si.

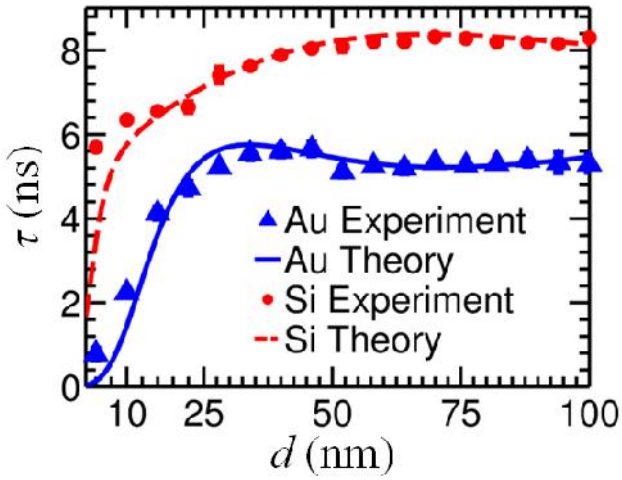

Figure 4.4.6: Theoretical and experimental values of fluorescence lifetime as a function of the distance *d* for QDs.

$$f(z) = \frac{\pi\left(r^2 - z^2\right)}{\frac{4\pi}{3}r^3} = \frac{3}{4}\frac{r^2 - z^2}{r^3}, \qquad -r \prec z \prec r. \tag{4.2.2}$$

The fluorescence signal from a dye molecule at height *z* is given by:

$$\S(z,t) = \S_0 e^{-t/\tau(z)}, \tag{4.2.3}$$

where $\tau(z)$ is the fluorescence lifetime of the dye molecule at height *z*.

This means that the total temporal dependence produced by the entire fluorescent sphere located at height *d* above the sample is given by:

$$I(t,d) = (f * \S)[d] = \S_0 \int_{-r}^{r} \frac{3}{4} \frac{r^2 - \P^2}{r^3} e^{-t/\tau(d-\P)} d\P . \tag{4.2.4}$$

According to Eq. (4.2.1), the average convolved fluoresence lifetime, $\tau_{conv}(d)$, can be calculated as:

$$\tau_{conv}(d) = \frac{\int_0^\infty t\, I(t,d)\, dt}{\int_0^\infty I(t,d)\, dt} = \frac{(f * \tau^2)[d]}{(f * \tau)[d]}. \tag{4.2.5}$$

For comparison, we also considered the unconvolved case where we assume all fluorophores are at the center of the spheres. For the case of nanospheres on gold, the difference between the two cases is small (~7.9% at most). But the assumption of a uniform fluorophore distribution does improve the agreement between theory and experiment. For the case of nanospheres on silicon, assuming a uniform fluorophore distribution generates much less modification (2.2% at most). Due to small QD sizes, spatial convolution was not performed in their theoretical calculations.

For the nanospheres, we found the quantum yield *q* to be 25% and 23% for the silicon and gold substrates, while τ_0 was determined to be 3.8 ns and 3.84 ns, respectively. For the QDs, τ_0 was 8.2 ns for the silicon wafer and 7 ns for gold film, while *q* was 35% for both substrates.

These results validate our expectation that for a given fluorophore and LbL film, its quantum yield q and intrinsic lifetime τ_0 should be independent of the underlying substrate. A more interesting possibility, however, is that we can use the self-assembled fluorophores to quantify the modification of PDOS in the vicinity of a complex dielectric or plasmonic nanostructures [24]. In this approach, we can first calibrate the fluorophore by extracting its q and τ_0 using a simple planar structure such as a silicon wafer. Then, we place the same fluorophore in close proximity to the nanostructure of interest, measure its fluorescence lifetime, and then use the lifetime to extract PDOS modification by the nanostructure. To validate the feasibility of this approach, we use the silicon wafer as our calibration sample (to extract q and τ_0) and the gold substrate as our test sample .

In the homogeneous medium, LbL film, the decay rate, b_0, without the presence of any interface can be divided into two components, as follows:

$$b_0 = b_{r0} + b_{nr}, \tag{4.2.6}$$

where b_{r0} is the radiative decay rate in the homogeneous medium, while b_{nr} is the intrinsic nonradiative decay rate of a fluorophore which is always constant. Substituting of Eqs. (3.1.7) and (3.2.16) into Eq. (4.2.6), we get:

$$b_0 = C\,°_0(\mu) + (1-q)b_0, \tag{4.2.7}$$

where $C = 2\mu|\mathbf{\mu}|^2 / 3\hbar£_0$ and $°_0(\mu)$ is the PDOS in the homogeneous medium. Simplifying Eq. (4.2.7) to be:

$$b_0 = \frac{C}{q}\,°_0(\mu). \tag{4.2.8}$$

In the presence of a substrate, the decay rate, b, can be written as:

$$b = b_r + b_{nr}, \tag{4.2.9}$$

where b_r is the radiative decay rate in the presence of a substrate. Similarly, Eq. (4.2.9) can be written in another form to be:

$$b = C \cdot (d, \mu) + (1-q) b_0, \tag{4.2.10}$$

where $\cdot(d, \mu)$ is the PDOS in the presence of a substrate. Substituting of Eq. (4.2.8) into Eq. (4.2.10), to find:

$$b = b_0 \left\{ 1 - q \left[1 - \frac{\cdot(d, \mu)}{\cdot_0(\mu)} \right] \right\}. \tag{4.2.11}$$

Comparing Eqs. (4.2.11) and (3.1.28), we find:

$$\frac{\cdot(d, \mu)}{\cdot_0(\mu)} = 1 - Z_{//}. \tag{4.2.12}$$

Using the definition that, the spontaneous emission lifetime of the dipole parallel to the interface is defined as the inverse of the decay rate, Eq. (4.2.11) can be written as:

$$\frac{\cdot(d, \mu)}{\cdot_0(\mu)} = 1 - \left[\frac{1}{q} \left(1 - \frac{\tau_0}{\tau} \right) \right]. \tag{4.2.13}$$

In our approach, q and τ_0 are extracted from the silicon wafer "calibration", τ is the fluorescent lifetime measured using the gold substrate, and $\rho(d,\omega)$ / $\rho_0(\omega)$ is the normalized PDOS in the presence of the gold substrate.

Fig. (4.4.7) plots the theoretical predictions for the normalized PDOS, $\rho(d, \omega)$ / $\rho_0(\omega)$, calculated by Eq. (4.2.12) at the emission peaks of the emitters. The triangles and squares are the experimental PDOS obtained via Eq. (4.2.13). The nanosphere data reproduce the expected PDOS with high accuracy (<10% error), while the QD data show equally good agreement only for distances shorter than 20-25 nm. This is likely due to the effects of the substrates on the multi-exponential fluorescence dynamics in the QDs, which is not

taken into account in our model. In any case, for many applications involving plasmonic excitations, the extreme near-field region (<20 nm) is of the greatest interest.

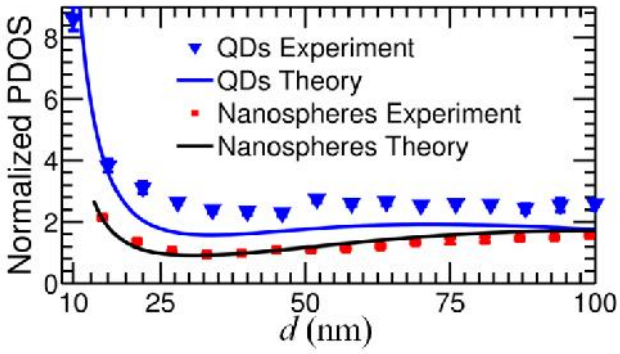

Figure 4.4.7: Theoretical and experimental results showing normalized PDOS as a function of the distance *d* for fluorescent nanospheres and QDs on gold.

4.5 Conclusion

We used LbL self-assembly to control the nanoscale distance between the fluorophores and planar optical structures for the study of spontaneous emission modification induced by the change in PDOS. Modification in the fluorescence lifetime of the self-assembled fluorophores agrees well with theoretical predictions. We found the intrinsic quantum yield q and fluorescence lifetime τ_0 of a fluorophore are independent of its surrounding medium. Furthermore, we demonstrated that it is possible to extract q and τ_0 using a planar substrate such as a silicon wafer, and then use the measured fluorescent lifetime to experimentally quantify PDOS modification in another optical micro- or nano- structure. For a gold substrate that supports plasmonic excitations, the relative deviation between the theoretically predicted PDOS and the experimentally measured results can be measured with less than 10% deviation.

References

1. S. Noda, M. Fujita, and T. Asano, Nature Photon. **1**, 449 (2007).
2. G. Q. Liu, Y. B. Liao, S. J. Ma, Y. F. Shen, and Z. Q. Ye, J. Opt. Soc. Am. B. **27**, 1942 (2010).
3. D. Englund, D. Fattal, E. Waks, G. Solomon, B. Zhang, T. Nakaoka, Y. Arakawa, Y. Yamamoto, and J. Vuckovic, Phys. Rev. Lett. **95**, 13904 (2005).
4. V. K. Komarala, Y. P. Rakovich, A. L. Bradley, S. J. Byrne, Y. K. Gun'ko, N. Gaponik, and A. Eychmueller, Appl. Phys. Lett. **89**, 253118 (2006).
5. C. W. Chen, C. H. Wang, C. M. Wei, and Y. F. Chen, Appl. Phys. Lett. **94**, 71906 (2009).
6. M. D. Birowosuto, S. E. Skipetrov, W. L. Vos, and A. P. Mosk, Phys. Rev. Lett. **105**, 13904 (2010).
7. Z. Jacob, J. Y. Kim, G. V. Naik, A. Boltasseva, E. E. Narimanov, and V. M. Shalaev, Applied Physics B-Lasers and Optics. **100**, 215 (2010).
8. J. M. Gerard, and B. Gayral, J. Lightwave Technol. **17**, 2089 (1999).
9. W. H. Chang, W. Y. Chen, H. S. Chang, T. P. Hsieh, J. I. Chyi, and T. M. Hsu, Phys. Rev. Lett. **96**, 117401 (2006).
10. R. F. Oulton, V. J. Sorger, T. Zentgraf, R. Ma, C. Gladden, L. Dai, G. Bartal, and X. Zhang, Nature. **461**, 629 (2009).
11. L. Novotny, B. Hecht, *Principles of Nano-Optics*, 1st edition, (Cambridge University, New York, 2006).
12. W. L. Barnes, Journal of Modern Optics. **45**, 661 (1998).

13. H. Kuhn, J. Chem. Phys. **53**, 101 (1970).

14. J. Y. Zhang, X. Y. Wang, and M. Xiao, Opt. Lett. **27**, 1253 (2002).

15. B. C. Buchler, T. Kalkbrenner, C. Hettich, and V. Sandoghdar, Phys. Rev. Lett. **95**, 063003 (2005).

16. K. Ray, R. Badugu, and J. R. Lakowicz, Chem. Mater. **19**, 5902 (2007).

17. A. Tulpar, Z. Wang, C. Jang, V. Jain, J. R. Heflin, and W. A. Ducker, Nanotechnol. **20**, 155301 (2009).

18. K. Itano, J. Y. Choi, and M. F. Rubner, Macromol. **38**, 3450 (2005).

19. W. Kern, and D. A. Poutinen, RCA Rev. **31**, 187 (1970).

20. G. Schlegel, J. Bohnenberger, I. Potapova, and A. Mwes, Phys. Rev. Lett. **88**, 137401 (2002).

21. J. R. Lakowicz, *Principles of Fluorescence Spectroscopy*, 3rd edition. (Springer, New York, 2006).

22. E. D. Palik, *Handbook of Optical Constants of Solids*, Vol. II (Academic Press, San Diego, 1985).

23. M. A. Green, and M. J. Keevers, Progress in Photovoltaics. **3**, 189 (1995).

24. A. F. Koenderink, M. Kafesaki, C. M. Soukoulis, and V. Sandoghdar, Opt. Lett. **30**, 3210 (2005).

Chapter 5

Characterization and Development of Active and Tunable Plasmonic Systems

5.1 Introduction

As discussed in previous Chapters, the Purcell effects have been widely used in the design and engineering of photonic bandgap materials [1], plasmonic nanostructures [2], high Q optical cavities [3], cavity quantum electrodynamics [4], and meta-materials [5]. Up to date, most studies focus on using Purcell effects to design appropriate nanostructures in order to achieve desired photon emission characteristics. In this Chapter, we will present a new application of Purcell effects, where we use the PDOS-induced fluorescent lifetime changes to characterize swellable polymers. Furthermore, we will present a proof-of-principle study on the feasibility of using such swellable polymers to construct tunable and active plasmonic systems.

As demonstrated in the previous Chapter, the emission dynamics of a fluorophore in the vicinity of a plasmonic nanostructure can depend critically on the distance between the fluorophore and the nanostructure. However, in order to measure the distance with nanoscale resolution, we must overcome the difficulty that Purcell effects are highly structurally dependent. In present Chapter, by using a simple plasmonic structure ─ a

planar Au film, we demonstrate that it is possible to directly link fluorescence lifetime with the local PDOS, and then use the modified PDOS to measure nanoscale morphological changes.

As a non-contact method for nanoscale characterization, our approach can have significant advantages in applications that involve deformable nanostructures such as swellable polymer films fabricated through LbL self-assembly. The swelling/deswelling of LbL film is a relatively recent discovery [6]. Based on the polymeric materials and the solutions pH values used during the self-assembly process, the thickness of a swellable film can be dynamically changed by up to 600% [7]. Given this unique behavior, such swellable polymers have found numerous applications such as, controlling cell proliferation and attachment [8], drug release [9], and hysteretic gating [10]. The dynamical changes of such swellable films are typically investigated using methods such as AFM. However, such contact-based methods typically rely on near-field probe-sample interactions to measure nanoscale morphological changes, which can lead to significant drawbacks in the study of swellable films. As a specific example, AFM can detect changes in the total thickness of the LbL film, but it would be almost impossible to study how individual polymer monolayer behaves within the multilayer structure. In contrast, with further development, our Purcell-effect-based method should be able to "see" within the swellable film and observe behaviors of individual monolayers. As a proof-of-concept demonstration, in this Chapter we investigate a deformable LbL system that has been well-characterized in several existing studies [10]. Yet even in this case, we find that the swelling/deswelling behavior of a single polymer monolayer is distinctively different from a LbL film with three monolayers, which is a phenomena that, to the best of our

knowledge, has not been previously reported.

Next, we use the swelling / deswelling of LbL films to tune the separation between gold nanoparticles and a monolayer of fluorescent dyes. Our experimental results show that by tuning the thickness of the LbL film, we can significantly modify the fluorescence lifetime of the dyes. This study demonstrates that it is possible to construct tunable and active plasmonic nanostructures using these swellable polymers.

5.2 Samples Fabrication

The pH-induced swellable LbL films were fabricated using the procedure illustrated in Fig. (5.2.1). To initiate self-assembly, we immersed a glass slide covered with a 100 nm thick gold film in a thiol solution (MHDA, 1 mM, pH ~ 2) for 24 hours, followed by ethanol sonication and DI water rinsing. During this step, a monolayer of ω-COOH thiol is adsorbed onto the gold film to form a negatively charged layer. Afterwards, we immersed the negatively charged sample in PAH aqueous solution (2 mg/ml, pH ~ 9.3). Due to electrostatic interaction, a positively charged PAH monolayer was deposited over the thiol group. Then, after rinsing in DI water of pH ~ 9.3, we immersed the sample in PSS aqueous solution (3 mg/ml, pH ~ 9.3) to deposit a negatively charged PSS monolayer over PAH. This deposition process can be repeated many times to build PAH/PSS bilayers one monolayer at a time. The only difference between this LbL self-assembly process and that one described in the previous Chapter is that the pH values of the polymeric solutions and rinsing water were adjusted during the self-assembly process to ~ 9.3 to ensure significant film swelling and deswelling [7,10]. During the study of using Purcell effect to measure nanoscale morphological changes, we consider two

types of swellable films, a single PAH monolayer on Au, and three monolayers (PAH/PSS/PAH) on Au. Finally, we immersed the samples in a solution of negatively charged CdSe/ZnS core/shell QDs (NN-LABS, emission peak at 621 nm, mean diameter 5 nm). In the next step, we could use the fluorescence signals generated by these QDs to characterize the thickness of the LbL film.

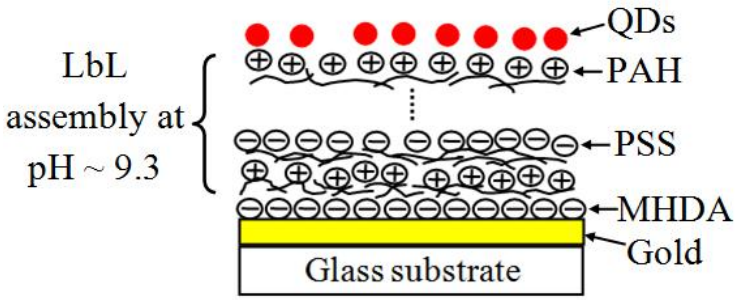

Figure 5.2.1: Schematic of the LbL self-assembly of swellable film that acts as a spacer between QDs and gold substrate.

Another sample we considered in this Chapter is illustrated in Fig. (5.2.2). It consists of a monolayer of Texas Red (TR) dye assembled over a glass substrate, followed by multiple bilayers of swellable polymers, and capped with gold nanoparticles. To fabricate this sample, we first cleaned a glass substrate [11] by immersing it in a 1:1:5 solution of $NH_4OH:H_2O_2:H_2O$ at 70 ^oC for 20 min, followed by immersion in a 1:1:6 solution of $HCl:H_2O_2:H_2O$ at 70 ^oC for additional 5 min. After each immersion step, the glass substrate was rinsed with DI water. During the cleaning process, OH^- ions of the used cationic solution were bounded to the glass surface to form a negatively charged layer that initiated LbL self–assembly deposition.

In order to self-assemble the uncharged TR (Sigma-Aldrich, emission peak at 620 nm)

dyes on the charged glass substrate, we conjugated TR to the polycation PAH following the method in Ref. [12]. Afterwards, when we immersed the negatively charged glass substrate in aqueous solution of TR-PAH, a monolayer of positively charged TR-PAH was deposited over the glass substrate. Then we consecutively immersed the sample in PSS and PAH aqueous solution at pH ~ 9.3 till we fabricated five PSS/PAH bilayers capped with PAH. Between and after each immersion step, the glass slide was rinsed with DI water at pH ~ 9.3. Finally, we immersed the sample in aqueous suspension of negatively charged gold nanoparticles (Purest Colloids, 3 nm diameter) to assemble these nanoparticles above the final PAH layer.

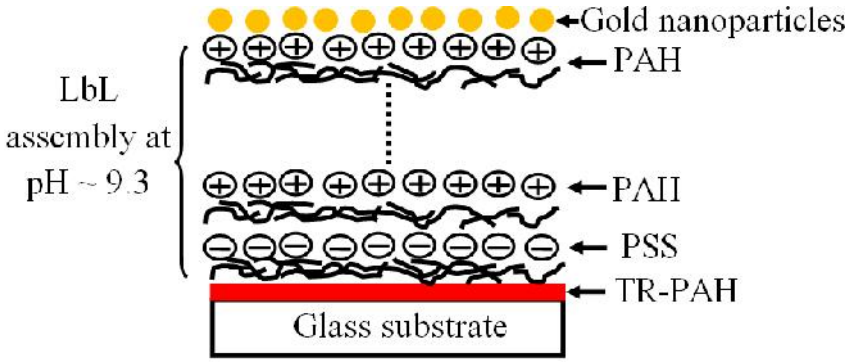

Figure 5.2.2: Schematic of the LbL self-assembly of swellable film that acts as a spacer between gold nanoparticles and TR dyes.

The swelling / dswelling studies were carried out by placing the samples in a cuvette containing aqueous solutions with the desired specific pH values, as shown in Fig. (5.2.3). Photoluminescence was measured using the TCSPC system described in previous Chapters. The fluorophores were excited using a picoseconds diode laser (model BDL-473-C from Becker and Hickl) which produces laser pluses at 473 nm, 40 ps in pulse width, and 20 MHz in repetition rate.

The swelling / deswelling of the LbL typically exhibit hysteresis. To record film thickness during the swelling / deswelling cycle, the pH of the aqueous solution in the cuvette was sequentially reduced from high to low values for the swelling cycle, and vice versa for the deswelling cycle. At each pH value of the cuvette solution, photoluminescence was measured typically 10 minutes after placing the sample in the pH-adjusted solution.

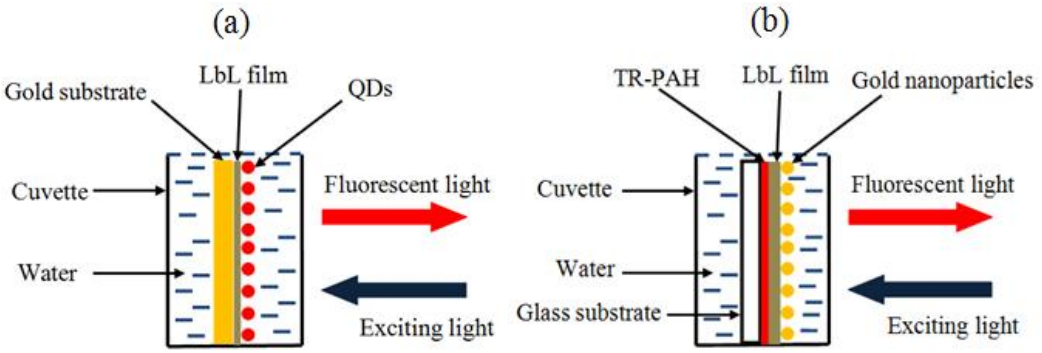

Figure 5.2.3: Photoluminescence measurements of (a) QDs and (b) TR in case of using pH-induced swellable LbL film.

5.3 Results and Discussions

The results in the Chapter 4 shows that the fluorescence dynamics of the self-assembled QDs can vary significantly depending on the thickness of PAH/PSS bilayers between the fluorophores and the Au substrate. In particular, as shown in Fig. (4.4.6), if the distance d between the QDs and the Au substrate is relatively small (<40 nm), the QD fluorescence lifetime decreases monotonically as the value of d decreses. Hence we can treat the relationship between the average lifetime τ and the distance d as a look-up table, where an experimentally measured lifetime τ is directly linked with a LbL film thickness d. In

this approach, we can rely on the PDOS-induced lifetime changes to quantify the morphological changes of the swellable polymers with nanoscale resolution.

To validate this approach, we first carried out a direct comparison with ellipsometry measurements. In this study, we used four LbL film samples with different PAH/PSS bilayer numbers. They were assembled according to the procedure described in Chapter 4, where we used pH ~ 7 during assembly. Both the lifetime measurements and ellipsometry measurements are carried out in air, not in cuvette.

The procedure for thickness measurement is starting with calculating the experimental average QDs fluorescence lifetime by using Eq. (4.2.1). Equation (4.2.13) shows that, in the vicinity of the plasmonic film, the average lifetime depends on the intrinsic fluorescence lifetime τ_0, the quantum yield q, and the modified PDOS, and can be rewritten as:

$$\tau = \tau_0 / \left\{1 - q\left[1 - \gamma(d)\right]\right\}, \tag{5.3.1}$$

where the parameter γ accounts for changes in PDOS and is defined as $\gamma(d) = \rho(d)/\rho_0(d)$ where, $\rho(d)$ and $\rho_0(d)$ respectively represents the PDOS in the presence and the absence of the Au substrate, and d denotes the distance between the fluorophores and the gold substrate. For planar substrate, the value of γ can be analytically calculated using Eq. (4.2.12). It should be emphasized that γ is essentially the Purcell factor and that its value depends only on the wavelength, the dielectric constants of the surrounding media, and fluorophore location. The value of γ, however, does not depend on specific fluorophores. For Au substrate, the theoretically predicted is shown in Fig. (5.3.1). Using this theoretical curve and setting q = 35% and τ_0 = 7 ns, obtained in

Chapter 4, we can treat Eq. (5.3.1) as a look-up table and directly link the measured lifetime with LbL film thickness *d*.

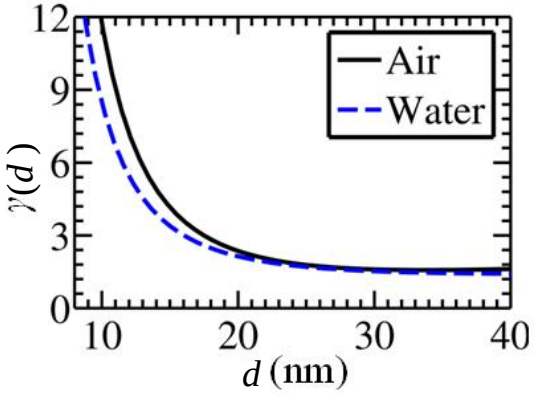

Figure 5.3.1: Change of PDOS as a function of the distance *d* between a fluorophore and the planar Au substrate when the upper medium is air (solid line) or water (dashed line).

In Fig. (5.3.2), we show the experimentally measured QD photoluminescence on four LbL samples with different film thickness *d*,assembled at pH ~ 7. In Fig. (5.3.3), we show film thicknesses extrapolated using the method outlined above, d_{PDOS}, versus the values obtained using ellipsometry, d_{Ellip}, for the four samples.

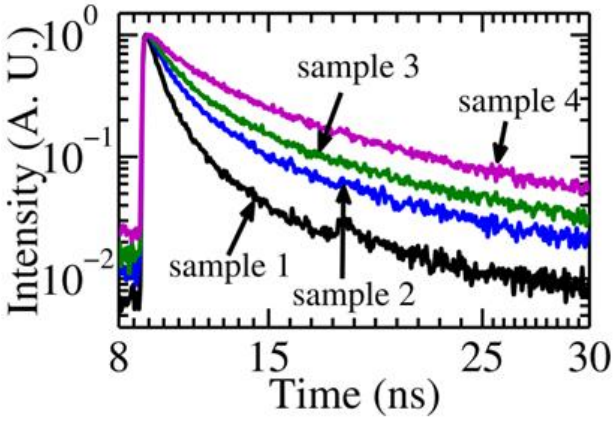

Figure 5.3.2: Experimental QD photoluminescence produced by four samples with different LbL film thickness *d*.

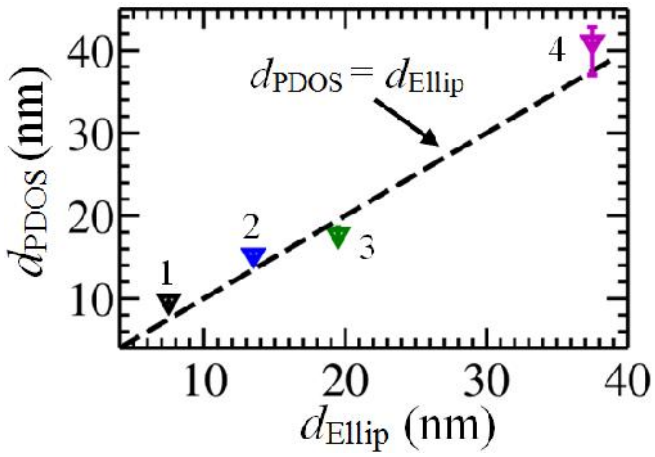

Figure 5.3.3: Comparison between LbL film thicknesses extrapolated using Purcell effect and those measured using ellipsometry.

Note that in our Purcell-factor-based approach, there is no fitting parameter, where all values are obtained experimentally. The good agreement in Fig. (5.3.3) clearly suggests that our approach can measure LbL film thickness with nanoscale resolution.

After validation, we apply the PDOS-based approach to investigate the pH-induced swelling/deswelling behavior of two types of swellable films assembled at pH ~ 9.3. One LbL sample consists of a single PAH monolayer on gold, and the other contains three monolayers (PAH/PSS/PAH) on gold.

We begin our study with a control experiment that confirms any variation in fluorescence lifetime is not caused by changing the chemical environment surrounding the fluorophores. This study was carried out by self-assembling the QDs over a planar glass substrate (without any Au layer) coated with a single PAH monolayer, followed by experimentally measuring the average lifetime under three different pH values (~ 3, 6.1, and 10.5) of the cuvette solution. The experimental QDs photoluminescence curves measured under the three different conditions are nearly identical. Figures (5.3.4) and

(5.3.5) show an example of QDs photoluminescence curve at pH 6.1, and the average fluorescence lifetimes evaluated for the three conditions, respectively.

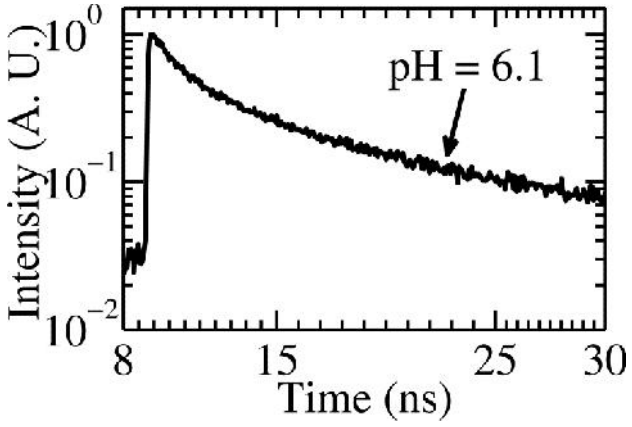

Figure 5.3.4: Fluorescence decay produced by QDs assembled above glass at pH ~ 6 of the cuvette solution.

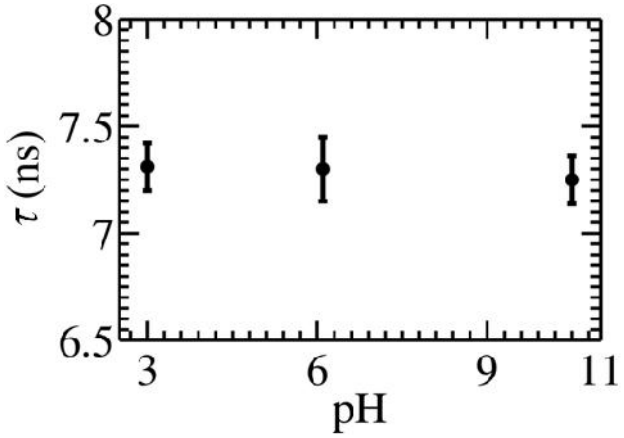

Figure 5.3.5: Average fluorescence lifetimes of QDs assembled over glass at different pH values of cuvette solution.

This study confirms that changing cuvette solution pH from 3 to 10.5 has no significant impact itself on QD fluorescence. This result is to be expected, since the refractive index of glass is very similar to that of the LbL film. Consequently, the change in lifetime due

to Purcell effects should be minimal, even though the distance between the QDs and the glass interface may substantially change due to PAH swelling/deswelling. As a result, in case of self-assembly above gold, any variations in fluorescence lifetime during the swelling/deswelling cycle can be attributed to the presence of the gold substrate and the changes in PDOS.

Figs. (5.3.6) and (5.3.7) show several representative examples of photoluminescence produced by QDs assembled above gold of the two LbL film samples measured at different pH values, respectively. One sample contains only a single PAH monolayer between the QDs and the gold substrate. The other sample contains three monolayers: PAH/PSS/PAH. It is clear that for both samples, QD fluorescence has significant dependence on the pH values of the aqueous solution. This fluorescence dynamics modification is due to the change of the LbL films thicknesses during the swelling/deswelling cycle.

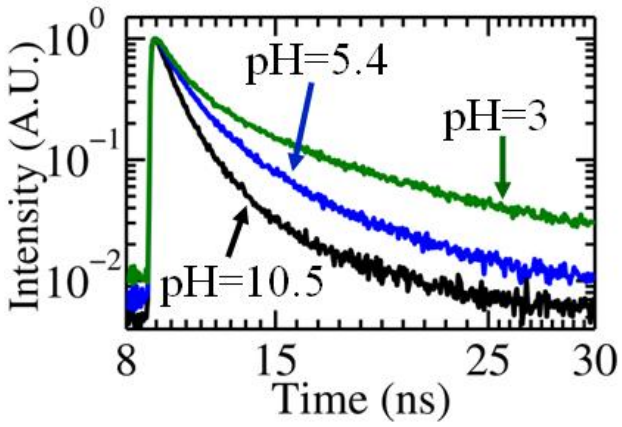

Figure 5.3.6: Fluorescence decay produced by QDs assembled above gold at different pH values of the cuvette solution for using a single PAH monolayer film and during the swelling cycle (pH decreases from 10.5 to 3).

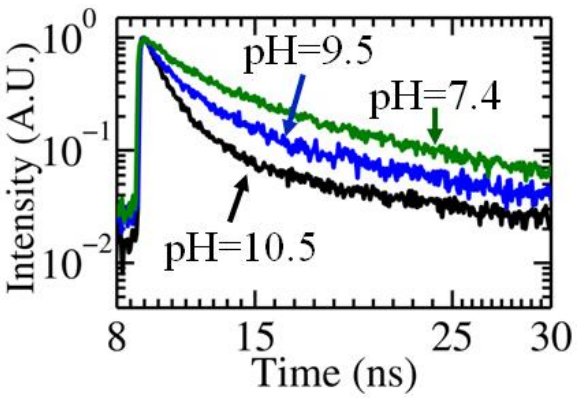

Figure 5.3.7: Fluorescence decay produced by QDs assembled above gold at different pH values of the cuvette solution for using PAH/PSS/PAH LbL film and during the deswelling cycle (pH increases from 3 to 10.5).

Figs, (5.3.8) and (5.3.9) respectively show the average QD lifetime for the one monolayer and the three monolayer samples as we adjust solution pH values. The hysteresis behavior is obvious: The change in QD average lifetime clearly depends on whether we decrease or increase solution pH values. Furthermore, these results also indicate that the

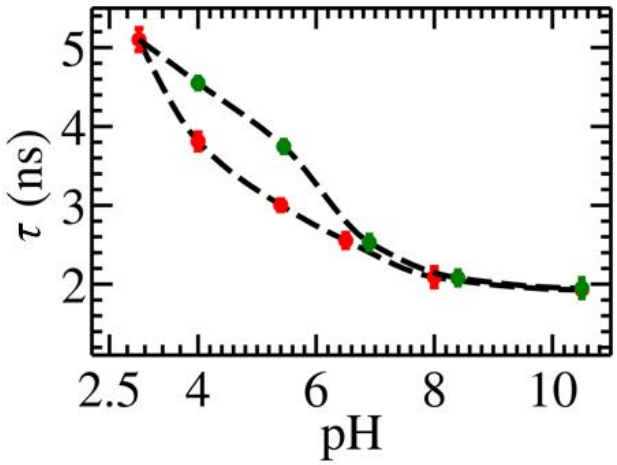

Figure 5.3.8: Fluorescence lifetime as a function of the pH of the cuvette solution for using PAH LbL film. The squares and circles represent data generated during swelling and deswelling cycles, respectively.

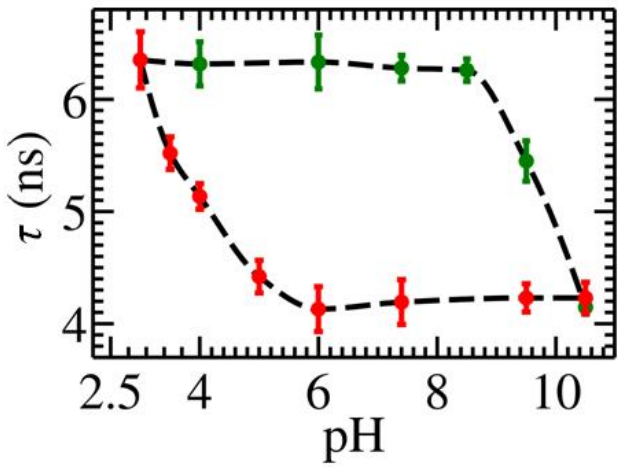

Figure 5.3.9: Fluorescence lifetime as a function of the pH of the cuvette solution for using PAH/PSS/PAH LbL film. The squares and circles represent data generated during swelling and deswelling cycles, respectively.

hysteresis of the one monolayer sample is much smaller than that of the three monolayer sample.

To quantify film hysteresis, we use Eq. (5.3.1) and the procedure outlined above to extrapolate the thickness of the swellable LbL films. The value of QD radius (2.5 nm) is subtracted from the total QDs-Au distance to ensure we only measure the thickness of the polymer LbL film. The results are shown in Figs. (5.3.10) and (5.3.11).

Again, it is quite clear that the one monolayer sample experiences much smaller hysteresis compared with the three monolayer sample. To the best of our knowledge, this behavior has never been reported in existing literature. The large hysteresis behavior shown in Fig. (5.3.11) is consistent with existing results in the literature. For example, similar large hysteresis swelling/deswelling behavior was obtained in Ref. 10 for PAH/PSS multilayers preassembled at pH 9.3 on a planar silicon wafer. We also note that in Fig. (5.3.11), the error bars for thicker film (d > 30 nm) are larger compared with the

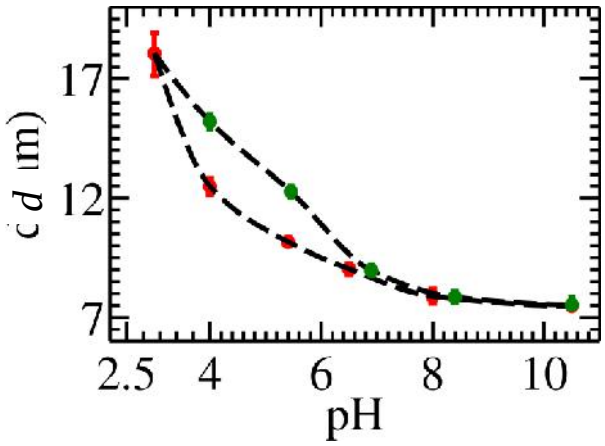

Figure 5.3.10: Thickness as a function of the pH of the cuvette solution of a monolayer PAH film. The squares and circles represent data generated during swelling and deswelling cycles, respectively.

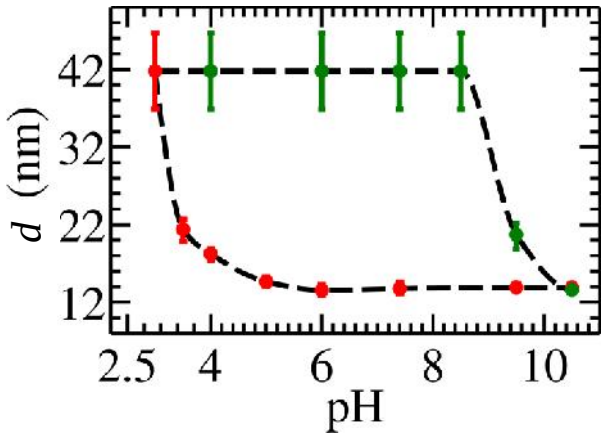

Figure 5.3.11: Thickness as a function of the pH of the cuvette solution of PAH/PSS/PAH LbL film. The squares and circles represent data generated during swelling and deswelling cycles, respectively.

results obtained with thinner film. This result can be explained by the fact that Purcell effects are much more pronounced in the extreme near-field case, as can be seen from Fig. (5.3.1). Hence at the larger distance, even a big change in film thickness may produce relatively small changes in average QD lifetime.

To further validate our thickness measurements based on PDOS-induced lifetime changes, we compared the thicknesses of two different swellable film samples obtained using two different approaches: one is our fluorescent lifetime based approach, and the other is liquid cell AFM measurements. Again, one swellable film contains only a single PAH monolayer, whereas the other is composed of PAH/PSS/PAH.

The AFM measurement procedure is as follows: First, we placed the sample in a liquid cell filled with pH adjusted aqueous solution. Then, we used AFM tip in contact mode at high pressure to remove part of the polymeric LbL film within the liquid cell. Afterwards, the same tip was used in tapping mode at very low pressure to image the height profile of the LbL film, including the removed part. The thickness of the swellable LbL film can be calculated by measuring the step depth between the normal and removed parts of the LbL film. Fig. (5.3.12-a) shows an example of AFM image taken to a 1 PAH film placed in a liquid cell at pH ~ 10.5 after removing part from the film. Fig. (5.3.12-b) shows the height profile along the red line indicated in Fig. (5.3.12-a). **(**The AFM images were taken by Moataz Bellah Khalifa in Dr. Heflin's group**).**

In Fig. (5.3.13), we show film thickness extrapolated using the fluorescence-lifetime-based method, $d_{\mathrm{PDOS,}}$ versus the values obtained using AFM, d_{AFM}. The results in Fig. 5.3.13 were obtained using four different combinations: two different swellable films (1 PAH and PAH/PSS/PAH) at two different pH values (pH 10.5 and 3). The good agreement in Fig. (5.3.13) clearly confirms that our approach can measure swellable LbL film thickness with nanoscale resolution.

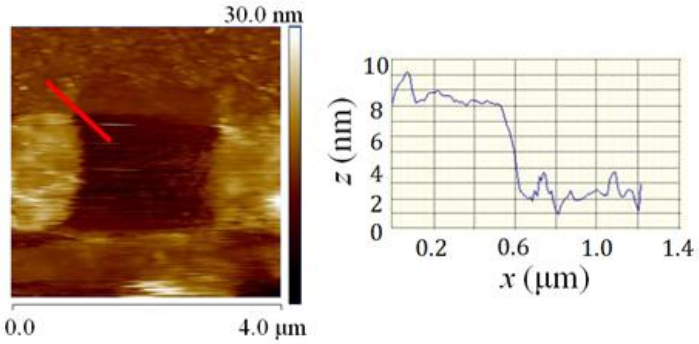

Figure 5.3.12: (a) Tapping mode AFM image of 1 PAH film in liquid cell at pH ~ 10.5 after removing a square part from it. (b) The height profile across the line, shown in Fig. (5.3.12.a), between the normal and removed parts in the film. *x* represents the horizontal distance change across the line and *z* is the corresponding LbL film height.

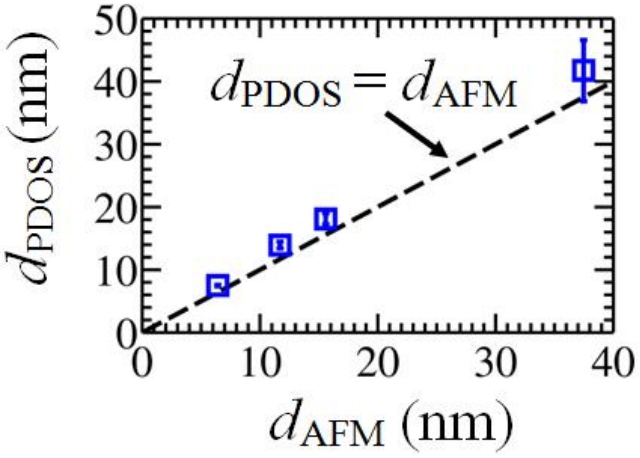

Figure 5.3.13: Comparison between LbL film thickness extrapolated using Purcell effect and those measured using AFM.

Fig. (5.3.11) shows that by changing solution pH values, we can tune the thickness of a LbL film by approximately 300%. Furthermore, we can easily incorporate optically active materials such as fluorescent QDs into the LbL film. Therefore, it is possible to utilize the swellable polymers to construct tunable and active plasmonic systems. For a

proof-of-concept demonstration, we first consider a relatively simple example, where we used a swellable film to control the fluorescence dynamics of TR dyes with plasmonic gold nanoparticles. Experimentally, this was achieved by monitoring the fluorescence lifetime of the TR dyes as we swell/deswell the LbL films.

Similarly, we started this study with a control experiment to show that any variation in fluorescence lifetime is not due to changing the chemical environment surrounding the TR dyes. This study was carried out by self-assembling TR-PAH monolayer over a negatively charged planar glass substrate (without gold nanoparticles deposition), followed by experimentally measuring the fluorescence lifetime under three different pH values (~ 3, 6, and 10.5) of the cuvette solution. The experimental TR dyes photoluminescence curves measured under the three different conditions are nearly identical. The fluorescence lifetimes are respectively 4.25 ± 0.05 ns for pH ~ 3, 4.27 ± 0.03 ns for pH ~ 6, and 4.32 ± 0.03 ns for pH ~ 10.5. This study confirms that changing cuvette solution pH from 3 to 10.5 has no significant impact itself on TR fluorescence.

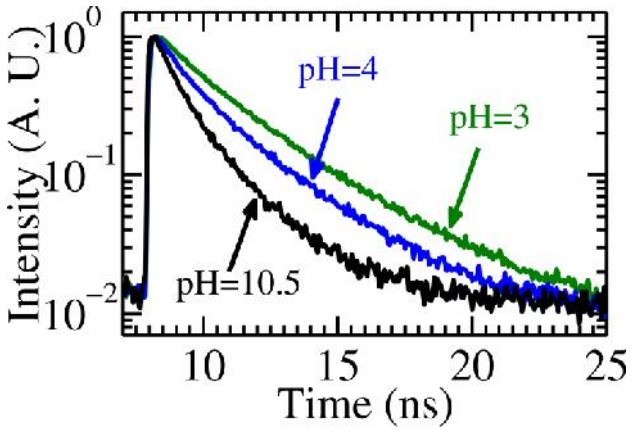

Figure 5.3.14: Fluorescence decay produced by TR dyes separated from gold nanoparticles by 5 PSS/PAH bilayers swellable film during the swelling process.

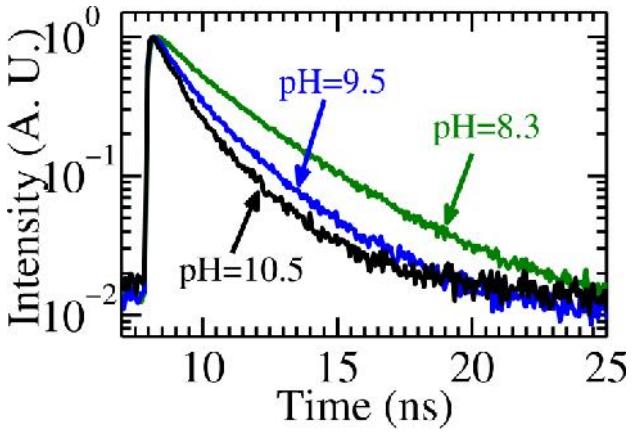

Figure 5.3.15: Fluorescence decay produced by TR dyes separated from gold nanoparticles by 5 PSS/PAH bilayers swellable film during the deswelling process.

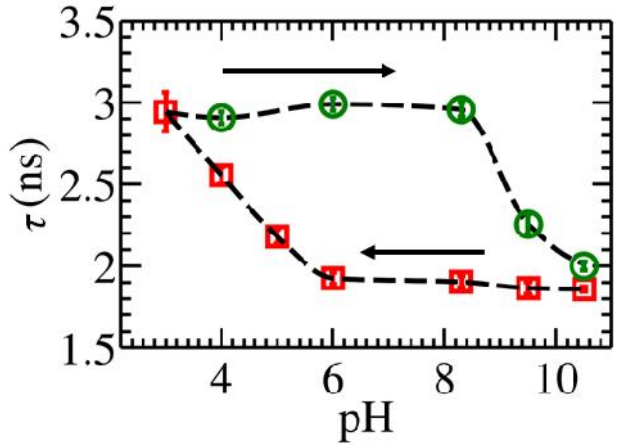

Figure 5.3.16: Fluorescence lifetime of TR dyes as a function of the pH of the cuvette solution. The squares and circles represent data generated during swelling and deswelling cycles, respectively.

Figs. (5.3.14) and (5.3.15) show several representative examples of photoluminescence produced by TR dyes separated from gold nanoparticles by 5 PSS/PAH bilayers swellable film during the swelling and deswelling processes, respectively. As can be observed, TR fluorescence has significant dependence on the pH values of the aqueous

solution.

Fig. (5.3.16) shows the fluorescence TR lifetime as we adjust cuvette solution pH values. As expected, the change in TR fluorescence lifetime clearly depends on whether we decrease or increase solution pH values. This result is also consistent with the large hysteresis obtained for PAH/PSS swellable films.

5.4 Conclusion

In conclusion, we reported a novel nanoscale measurement method based on Purcell effect to probe optical thickness changes of LbL polymer films. We found good agreement between the measurements obtained with our method and those with ellipsometry as well as liquid cell AFM measurements. Furthermore, we used this fluorescence-lifetime-based approach to characterize the swelling/deswelling behavior of PAH and PAH/PSS/PAH films. Our results indicate a significant difference in hysteresis dynamics between the two cases. Finally, we investigated a simple plasmonic system that exhibit both optical fluorescence and high tenability. We demonstrated that it is possible to significantly modify the fluorescence dynamics of TR dyes by tuning the separation between them and gold nanoparticles via the swelling/deswelling behavior of 5 PSS/PAH bilayers.

References

1. H. Iwase, D. Englund, and J. Vučković, Opt. Express. **18**, 16547 (2010).
2. A. G. Brolo, S. C. Kwok, M. D. Cooper, M. G. Moffitt. C. W. Wang, R. Gordon, J. Riordon, and K. L. Kavanagh, J. Phys. Chem. B. **110**, 8307 (2006).
3. J. P. Reithmaier, G. Sęk, A. Löffler, C. Hofmann, S. Kuhn, S. Reitzenstein, L. V. Keldysh, V. D. Kulakovskii, T. L. Reinecke and A. Forchel, Nature. **432**, 197 (2004).
4. J-M Gerard, and B. Gayral, J. Lightwave Technol. **17**, 2089 (1999).
5. K. Tanaka, E. Plum, J. Y. Ou, T. Uchino, and N. I. Zheludev, Phys. Rev. Lett. **105**, 227403 (2010).
6. J. D. Mendelsohn, C. L. Barrett, V. V. Chan, A. J. Pal, A. M. Mayes, and M. F. Rubner, Langmuir. **16**, 5017 (2000).
7. K. Itano, J. Choi, and M. F. Rubner, Macromolecules. **38**, 3450 (2005).
8. J. D. Mendelsohn, S. Y. Yang, J. Hiller, A. I. Hochbaum, and M. F. Rubner, Biomacromolecules. **4**, 96 (2003).
9. A. J. Chung, and M. F. Rubner, Langmuir. **18**, 1176 (2002).
10. D. Lee, A. J. Nolte, A. L. Kunz, M. F. Rubner, and R. E. Cohen, J. Am. Chem. Soc. **128**, 8521 (2006).
11. W. Kern, and D. A. Poutinen, RCA Rev. **31**, 187 (1970).
12. J. Kerimo, D. M. Adams, and P. F. Barbara, J. Phys. Chem. B. **102**, 9451 (1998).

Chapter 6

Characterizing the Impact of Micro- and Nano-lithography on the Fluorescence Dynamics of Self-Assembled Fluorophores

6.1 Introduction

Patterning polymeric thin films is highly relevant for numerous photonics applications [1-3]. For example, different techniques have been developed towards forming full color displays by defining red, green, and blue fluorescent patterns [4]. In addition, patterning organic fluorescent systems can be utilized to develop optical data storage devices [5,6]. Furthermore, fluorescent materials conjugated with polymer have also found applications in photoluminescent imaging [7], optical transducers [8], plastic lasers [9], and chemical sensors [10].

Several successful techniques have been developed in the literature to form fluorescent patterns using polymers. The most common approach is achieved by using acid-sensitive fluorescent dyes [11]. During this process, polymeric film containing a photoacid generator and an acid sensitive fluorescent dye are irradiated through a mask and the produced sample is heated to start the reaction of the fluorescent dyes with proton

in the irradiated area which result in modifications on the photoluminescent color. Other promising methods include photo-bleaching [12], photo-patterning using short wavelength ultraviolet (UV) light [13], and a hybrid approach that combines electrophoretic deposition and photolithography [14].

Much effort has been done to characterize the influence of different patterning processes on the optical properties of the used fluorophores. For instance, Christoph Kocher *et al*. [4] studied the change of photoluminescent spectrum of oriented photofunctional polymer when patterned by photobleaching using a white light source. They found that as the photobleaching time increases, the maximum photoluminescent intensity of the areas subjected to the white light decreases. Simultaneously, the fluorophores also display blue-shift. Also, the impact of UV light on various fluorescent polymers has been investigated by observing the changes in the fluorescence spectra of the regions subjected to UV exposure [15,16]. A soft-molding lithography technique has also been developed to pattern functional biomacromolecules embedded in hydrogels without changing the optical properties of the fluorescent proteins [17].

To the best of our knowledge, the impact of various lithography techniques on the fluorescence lifetime of different fluorophores has not been extensively studied. Yet for many applications, especially those involving active processes such as fluorescence, stimulated emission, and lasing, any change in fluorescence dynamics, especially reduction in quantum yield, can become a very important factor [18,19]. Here our goal is to investigate the impact of several commonly used lithography techniques on the fluorescence of QDs and dyes. Specifically, we study the process of thermal evaporation and removal of masking materials, micro- and nano-patterning through UV ablation and

FIB milling, and self-assembly over nanostructures.

Evaporating and etching sacrificial masks is a common lithography method. [20]. Here we first study the impact of this whole process on the fluorescence dynamics of two different types of fluorophores. Afterwards, we consider two different processes for micro- and nano-patterning of fluorescent polymeric films, one based on UV ablation and the other through FIB milling. Finally, we deposit fluorescent QDs over metallic structure and measure its fluorescence. With additional work, the results reported in this Chapter can serve as the first step towards incorporating fluorescent or gain media into patterned plasmonic nanostructures.

6.2 Impact of Evaporating and Etching

In this study we consider two types of fluorophores, one is self-assembled TR dyes (from Sigma-Aldrich, emission peak at 620 nm) and the other is CdSe/ZnS QDs (from NN–LABS, emission peak at 621 nm, 5 nm mean diameter). We first cleaned a glass substrate [21] by immersing it in a 1:1:5 solution of $NH_4OH:H_2O_2:H_2O$ at 70 ^oC for 20 min, followed by immersion in a 1:1:6 solution of $HCl:H_2O_2:H_2O$ at 70 ^oC for additional 5 min. After each immersion step, the glass substrate was rinsed with DI water. During the cleaning process, OH^- ions of the used cationic solution were bounded to the glass surface to form a negatively charged layer that initiates LbL self–assembly deposition.

In order to self-assemble the uncharged TR dyes on the charged glass substrate, we conjugated TR to the polycation PAH following the method in Ref. [22]. Afterwards, we consecutively immersed the negatively charged glass substrate in aqueous solutions of TR-PAH and polyanion PSS, with rinsing in copious amount of DI water between and

after each step, till we fabricated three monolayers of TR-PAH/PSS/TR-PAH LbL film. For samples containing QDs, we sequentially immersed the clean glass substrate in solutions containing PAH, PSS, and PAH, within DI water rinsing in between. Then, after fabricating three monolayers film composed of PAH/PSS/PAH, we immersed the sample in an aqueous suspension of the QDs to be attached by electrostatic force to the PAH topmost layer.

After drying the samples with nitrogen gas, a 30 nm aluminum layer was evaporated above the two samples by using e-beam evaporation. Then finally, we etched away the aluminum mask by immersing the samples in a 1 mM HCl aqueous solution for 2 hours at ~ 45 ^{o}C.

Figs. (6.2.1-a) and (6.2.1-b) show a comparison between the fluorescence decay of the self-assembled TR on glass before aluminum evaporation and after both evaporation and acid etching, respectively. As can be observed, the photoluminescence of TR is not significantly impacted by the Al deposition and removal, and remains single exponential. Figure (6.2.2) represents the fluorescence decay of the self-assembled QDs on glass before aluminum evaporation. However, we found that after aluminum etching, we can no longer detect any QD photoluminescence.

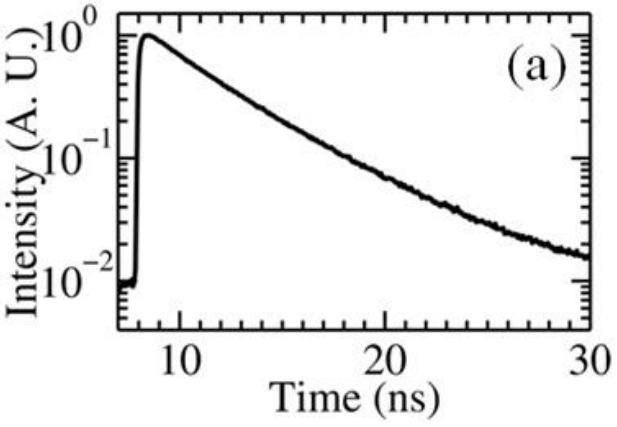

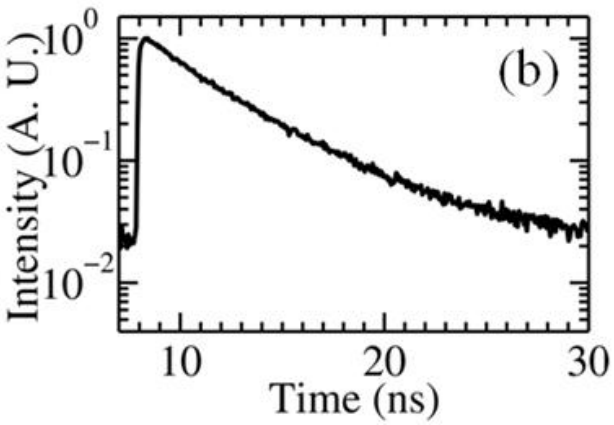

Figure 6.2.1: Fluorescence decay produced by TR assembled above glass (a) before aluminum evaporation and (b) after aluminum etching.

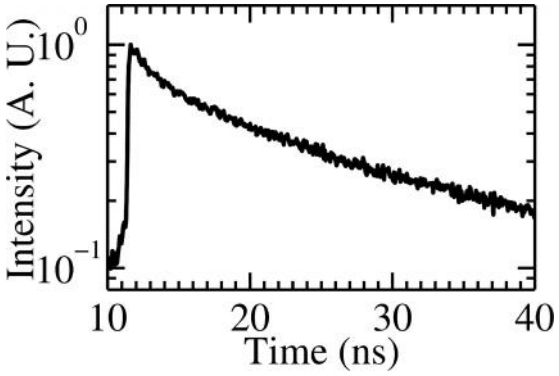

Figure 6.2.2: Fluorescence decay produced by QDs assembled above glass before aluminum evaporation.

Photoluminescence in each case was measured with TCSPC (Picoharp 300, PicoQuant) and a pulsed 473 nm laser diode (BDL-473-C, Becker and Hickl) for optical excitation. The average and standard deviation of fluorescence lifetime of TR was calculated, using single exponential fitting, from TCSPC measurements at 8 distinct locations on the same sample to be 4.03 ± 0.02 and 4.17 ± 0.02 ns before aluminum evaporation and after etching it, respectively. These results demonstrate that the process of evaporating and

etching aluminum can be safely used during patterning of self-assembled TR because it has a negligible effect on the fluorescence dynamics of TR.

The average QDs fluorescence lifetime τ was calculated by using $\tau^2 = \int_0^\infty t\, I(t)\, dt \Big/ \int_0^\infty I(t)\, dt$ where $I(t)$ is the experimental measured fluorescence intensity. Using the TCSPC measurements for QDs assembled above glass and before aluminum evaporation, τ was calculated to be 9.8 ± 0.07 ns. However, using aluminum mask to pattern fluorophores containing QDs may not be appropriate.

6.3 Patterning of Fluorescent LbL Films using UV Ablation

In this section, we consider the impact of UV ablation on TR and QDs. The first patterning process is illustrated schematically in Fig. (6.3.1). First, a cleaned glass substrate was immersed consecutively in aqueous solutions of TR-PAH and PSS (with DI water rinsing in between) till we fabricated three monolayers of TR-PAH/PSS/TR-PAH LbL film, Fig. (6.3.1-a). Then, after drying the sample, a 30 nm aluminum mask was patterned on the LbL film (refer to Fig. (6.3.1-b)) by using e-beam evaporation through a grid. Afterwards, we subjected the sample for 5 min to UV laser of 248 nm wavelength, 45 mJ/cm^2 fluence, and 3 Hz repetition rate to ablate the areas of the LbL film not covered by metal as shown in Fig. (6.3.1-c). Finally, we etched away the aluminum mask, Fig. (6.3.1-d), by immersing the sample in a 1 mM HCl aqueous solution for 2 hours at ~ 45 ^{o}C.

Fig. (6.3.2-a) shows a fluorescent image to the fabricated sample at the step shown in Fig. (6.3.1-b) taken by a Zeiss LSM 510 NLO + VIS confocal laser scanning microscope. The dark regions in this figure represent the areas covered with the aluminum layer, while, the

bright regions are the bare TR-PAH/PSS/TR-PAH LbL film. Similarly, Fig. (6.3.2-b) is a fluorescent image to the sample after using UV ablation and etching the aluminum. As

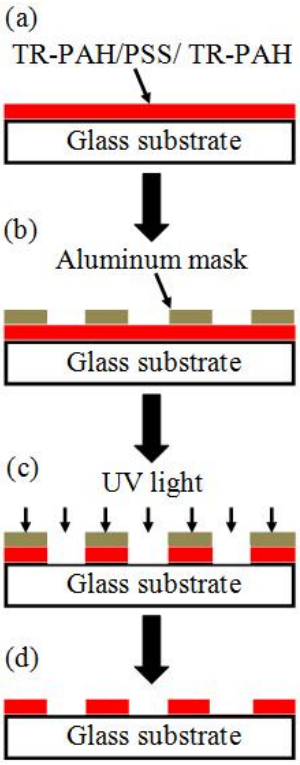

Figure 6.3.1: Schematic of TR dye patterning using UV ablation.

(a)

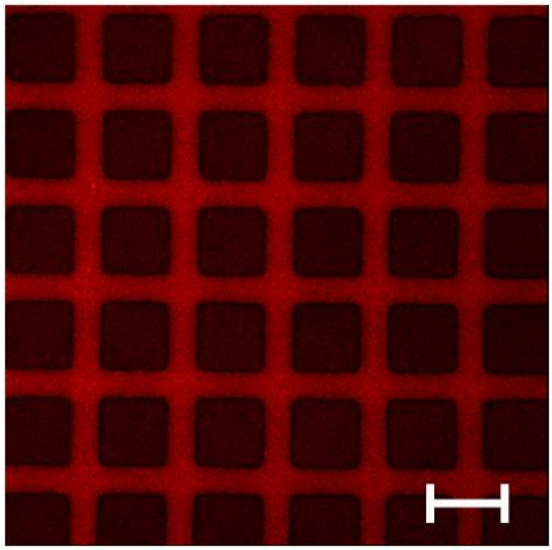

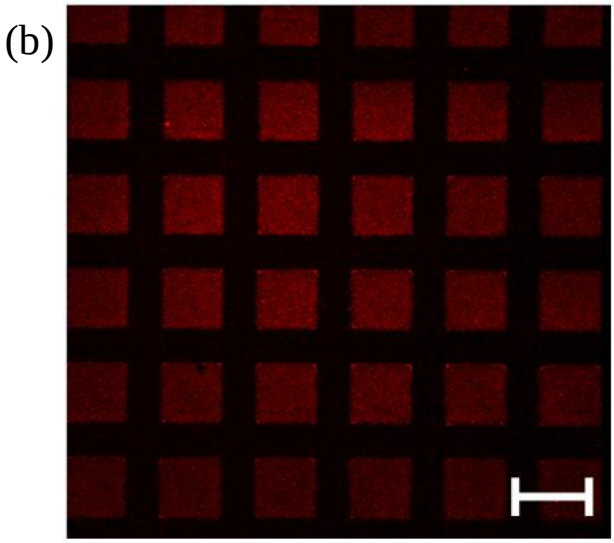

Figure 6.3.2: Fluorescent images to the fabricated sample in Fig. 6.3.1 that correspond to the steps (a) Fig. 6.3.1-b, and (b) Fig. 6.3.1-d. The length of the scalebars is 80 µm.

shown in this figure, the aluminum mask could protect the LbL film underneath from UV ablation step. As a result, these areas appear brightly in the fluorescent image of Fig. (6.3.2-b). On the other hand, the TR dyes exposed to UV laser (i.e., not covered with aluminum) are completely removed, as seen in Fig. (6.3.2-b).

Fig. (6.3.3) shows the fluorescence decay of the self-assembled TR after the step of UV ablation and etching the aluminum. The fluorescence lifetime of TR at this step was calculated from TCSPC measurements to be 4.18 ± 0.02 ns. These results demonstrate that patterning process based on UV ablation and aluminum mask does not appear to significantly shorten fluorescence lifetime. Indirectly, we can infer that this patterning method does not increase non-radiative recombination, which suggest that the quantum yield of TR dye is not reduced by this method.

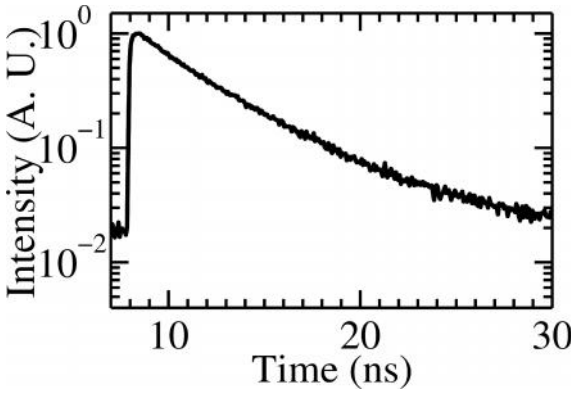

Figure 6.3.3: Fluorescence decay produced by TR assembled above glass after the whole patterning process.

A similar patterning process for the QDs is shown schematically in Fig. (6.3.4). In this method, a cleaned glass substrate was immersed consecutively in aqueous solutions of PAH and PSS, with rinsing in copious amount of DI water between and after each step, till we fabricated three monolayers of PAH/PSS/PAH LbL film. Afterwards, we exactly followed the same procedure described in Fig. (6.3.4). The end result is that after aluminum mask removal, the sample was covered by a patterned polymeric film capped with a positively charged PAH layer, as illustrated in Fig. (6.3.4-d). In the final step, we immersed the sample in the aqueous suspension of the QDs. Therefore, the QDs were attached by electrostatic force to the regions that covered only by the PAH/PSS/PAH LbL film, Fig. (6.3.4-e). Due to the electrostatic interaction, the QDs are predominately adsorbed onto the region containing PAH.

Fig. (6.3.5) shows a fluorescent image to the produced pattern using QDs as fluorophores. The dark regions in this figure represent the LbL film areas ablated using UV laser, while, the bright regions contain the attached QDs to the LbL film. The results in this figure demonstrate that it is possible to use UV ablation to place the QDs on the

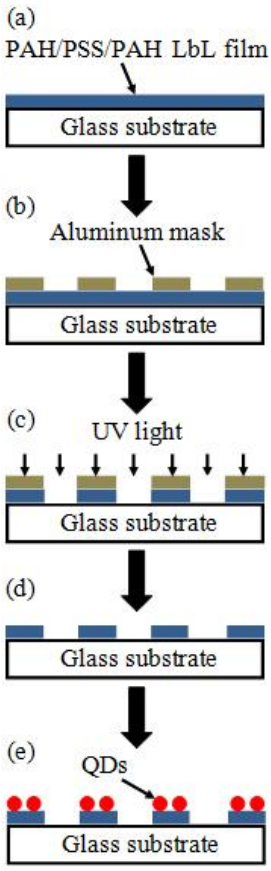

Figure 6.3.4: Schematic of QDs patterning using UV ablation.

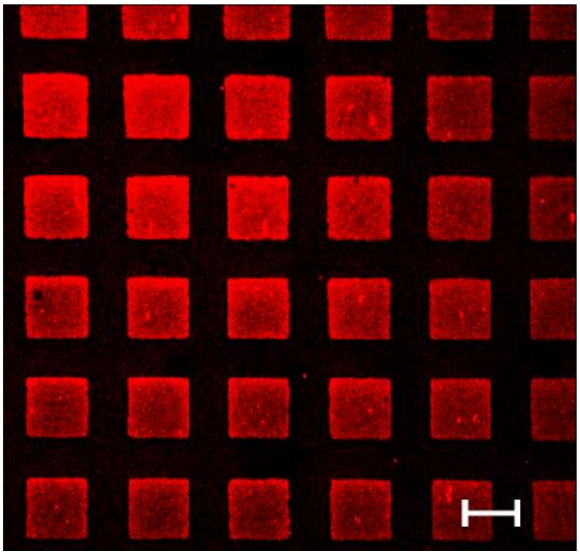

Figure 6.3.5: Fluorescent image to the patterned QDs. The length of the scalebars is 80 µm.

desired regions. Fig. (6.3.6) is the fluorescence decay of the used QDs assembled over the patterned PAH/PSS/PAH LbL film. Using the TCSPC measurements, τ was calculated to be 9.4 ± 0.15 ns. The main advantage of this patterning process is that the used QDs were not subjected to the process of aluminum evaporation and etching and therefore, it remains highly fluorescent with reasonable quantum yield.

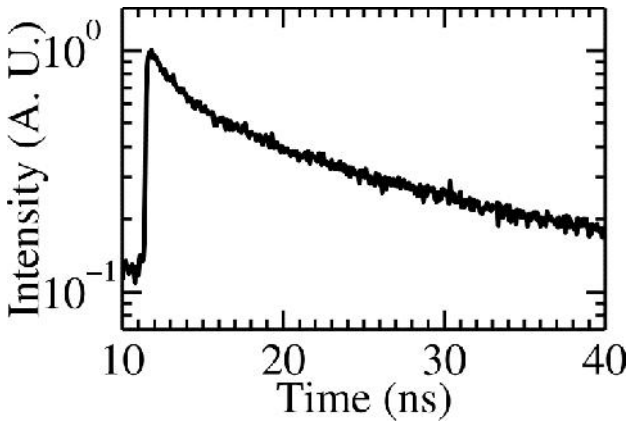

Figure 6.3.6: Fluorescence decay produced by QDs assembled over the patterned LbL film.

6.4 Patterning of Fluorescent Dyes using FIB

Here we considered FIB-based patterning of fluorescent materials. Similarly, a clean glass substrate was first immersed in TR-PAH aqueous solution to assemble a monolayer of TR-PAH over a glass surface. Afterwards, the sample was immersed consecutively in aqueous solutions of PSS and PAH till we self-assembled the desired number of PSS/PAH bilayers. Then, 30 nm aluminum layer was evaporated above the LbL film used to resolve the charging problem resulted from using the scanning electron microscope (SEM) combined with FIB. Finally, we used FIB to drill 300 nm diameter holes separated by 600 nm in the sample followed by etching away the aluminum layer.

Figs. (6.4.1-a) and (6.4.1-b) show SEM image to a patterned film consisting of TR-PAH + 75 PSS/PAH bilayers before etching the aluminum and AFM image to it after etching the aluminum, respectively.

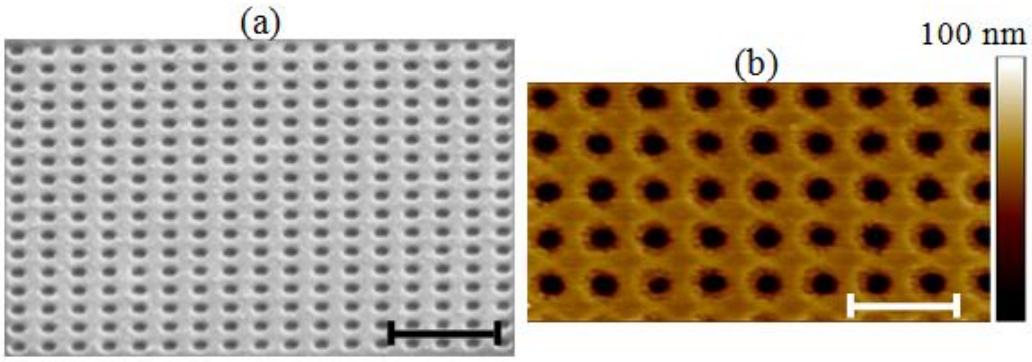

Figure 6.4.1: (a) Tilted SEM image to the patterned TR-PAH + 75 PSS/PAH LbL film before aluminum etching, and (b) AFM image to the same film after aluminum etching. The lengths of the scalebars are (a) 2 µm for horizontal distances, and (b) 1.2 µm.

Fig. (6.4.2-a), solid line, shows the fluorescence decay produced by TR covered with 75 PSS/PAH bilayers and 30 nm aluminum layer before patterning the sample. The fluorescence lifetime was calculated to be 2.72 ± 0.02 ns, which is less than that value of TR assembled above glass without the presence of the aluminum film. One possible explanation for the reduced fluorescence lifetime is the presence effect of the metallic film [24]: As we have shown in Chapter 4, the fluorescence lifetime should depend on the separation between the metallic film and the TR layer. For example, from TCSPC measurements, the average fluorescence lifetime of TR covered with 4 PSS/PAH bilayers and 30 nm aluminum layer was found to be 1.63 ± 0.07 ns.

The fluorescence decay produced by TR covered with patterned 75 PSS/PAH bilayers film and aluminum film is shown in Fig. (6.4.2-a), dashed line. This figure shows that the

patterned film using FIB could emit good fluorescent signal, however, the fluorescence lifetime was modified by the patterning process to be 1.84 ± 0.1 ns. For more verification, we etched away the aluminum film and recorded the fluorescence decay, Fig. (6.4.2-b), of the same pattern to give 1.8 ± 0.1 ns fluorescence lifetime. Therefore, we conclude that the FIB can be used to produce accurate fluorescent nano-pattern with good fluorescent intensity, however, it affects the fluorescence lifetime of TR. Indirectly, it suggests that FIB patterning may increase the non-radiative recombination of TR and correspondingly reduce their quantum yield.

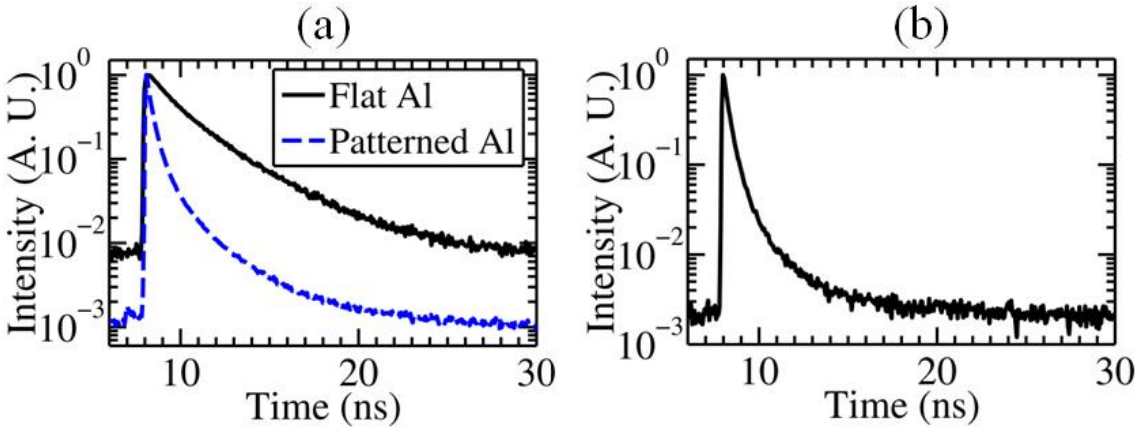

Figure 6.4.2: Fluorescence decay produced by TR under 75 PSS/PAH bilayers film and (a) 30 nm flat aluminum film (solid line), 30 nm patterned aluminum film (dashed line), (b) after etching the aluminum and in the same patterning place.

6.5 Self-Assembly of QDs over Plasmonic Nanostructures

Since the fluorescence dynamics of fluorophores are affected by the beams of the FIB, we recommend patterning the substrate first using FIB and then self-assemble the fluorophore to the substrate. This idea could be performed as follows: First, we used e-beam evaporation to fabricate 100 nm planar gold film on a glass substrate following the

same procedure described in Chapter 4. We then used FIB to drill nano-array which consists of 100 nm diameter holes separated by 500 nm on the gold substrate. Fig. (6.5.1-a) shows SEM image to the fabricated nano-array.

After fabricating the desired pattern using FIB on the substrate, we started the self-assembly process. The gold substrate was first immersed in a thiol solution (MHDA, 1 mM, pH ~ 2) for 24 hours, followed by ethanol sonication and DI water rinsing. During this step, a monolayer of ω-COOH thiol was adsorbed onto the gold film to form a negatively charged layer. Afterwards, the sample was immersed consecutively in aqueous solutions of PAH and PSS till we self-assembled the desired number of layers capped with PAH. Finally, we immersed the sample in a solution of negatively charged CdSe/ZnS core/shell QDs (NN-LABS, emission peak at 621 nm, mean diameter 5 nm) to be adsorbed on the LbL film by electrostatic force. Fig. (6.5.1-b) shows a fluorescent image to the QDs assembled above 4.5 PAH/PSS bilayers. The bright fluorescence generated by the nano-patterned region (corresponds to the central square in Fig. (6.5.1-b)) suggests that QDs remain highly fluorescent.

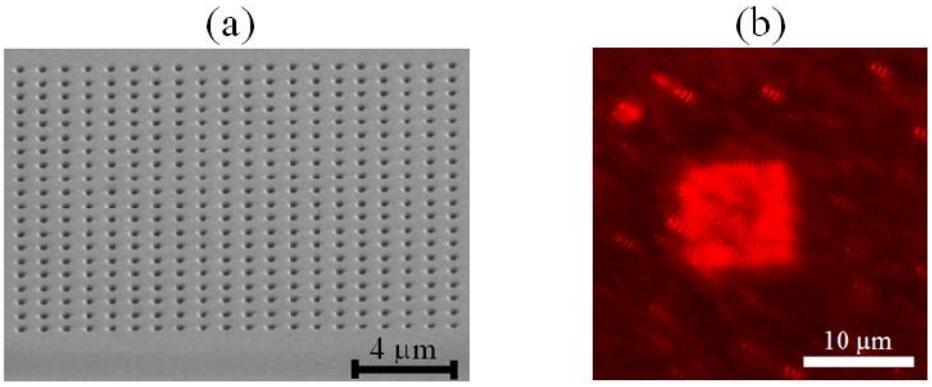

Figure 6.5.1: (a) Tilted SEM image to the patterned gold substrate. (b) Fluorescence image of the sample covered with QDs. The bright central square corresponds to the nanostructured region shown in (a).

Figs. (6.5.2-a) and (6.5.2-b) show the fluorescence decay produced by QDs assembled above 4.5 PAH/PSS bilayers film on flat and patterned gold substrates, respectively. Using the TCSPC measurements, τ was calculated to be 4.1 ± 0.08 ns and 3.98 ± 0.09 ns on flat and patterned gold substrates, respectively.

As a result, this patterning procedure can produce accurate pattern with bright fluorescence and it has a negligible impact on the fluorescence lifetime of the assembled fluorophores.

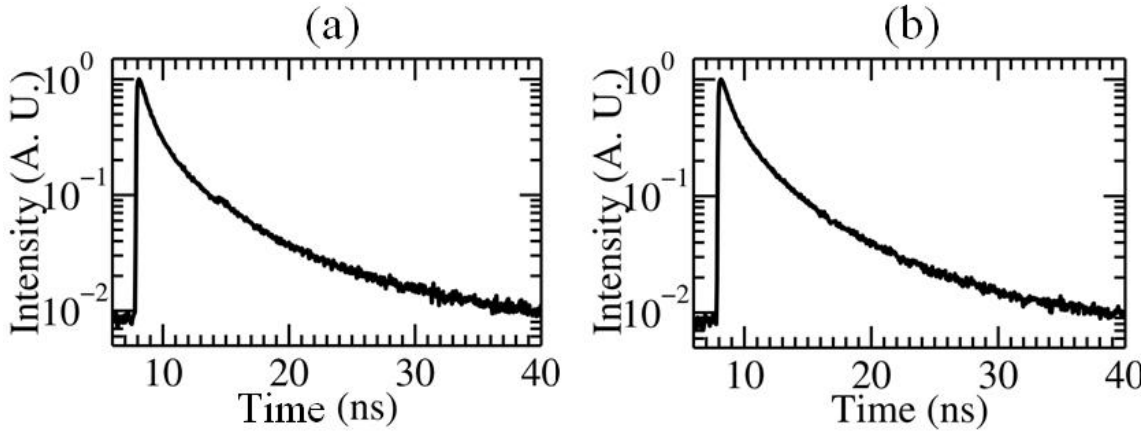

Figure 6.5.1: Fluorescence decay produced by QDs assembled above 4.5 PAH/PSS bilayers on (a) flat gild substrate, and (b) patterned gold substrate.

6.6 Conclusion

We evaluated the efficiency of different patterning methods of fluorophores attached to polymeric thin film by observing the accuracy of the produced pattern, the fluorescent signal emitted from it, and the fluorescence dynamics of the used fluorophores. We found that by using UV ablation and sacrificial aluminum masks, we can produce micron-scale patterns with high fluorescent intensity and reasonable quantum yield. On the other hand,

the FIB-based patterning process seems to reduce fluorescence lifetime of TR dyes, even though photoluminescence generated by the TR dyes remains. Finally, we found that self-assembly of QDs over plasmonic nano-patterns produces bright fluorescence compared with that observed on flat plasmonic surface. This self-assembly process has a negligible impact on the fluorescence lifetime of the assembled QDs.

References

1. M. Tomasulo, and F. Raymo, J. Mater. Chem. **15**, 4354 (2005).
2. L. Liu, K. Nakatani, R. Pansu, J. Vachon, P. Tauc, and E. Ishow, Adv. Mater. **19**, 433 (2007).
3. C. Pistolis, S. Boyatzis, M. Chatzichristidi, and P. Argitis, Chem. Mater. **14**, 790 (2002).
4. F. C. Kocher, A. Montali, P. Smith, and C. Weder, Adv. Func. Mater. **11**, 31 (2001).
5. K. Horie, S. Murase, S. Takahashi, and M. Teramoto, Macromol. Symp. **195**, 201 (2003)
6. K. D. Belfield, and K. J. Schafer, Chem. Mater. **14**, 3656 (2002).
7. J. Ohshita, T. Uemura, D. Kim, A. Kunai, Y. Kunugi, and M. Kakimoto, Macromolecules. **38**, 730 (2005).
8. M. Leclerc, Adv. Mater. **11**, 1491 (1999)
9. M. Zavelani-Rossi, M. Nisoli, S. DeSilvestri, G. Lanzani, C. Zenz, P. Mataloni, and G. Leising, Appl. Phys. Lett. **73**, 2860 (1998)
10. H. Tong, L. Wang, X. Jing, and F. Wang, Macromolecules. **36**, 2584 (2003).
11. S. Kim, and S. Park, Adv. Mater. **15**, 1342 (2003).
12. L. Gao, N. Lu, J. Hao, W. Hu, G. Shi, Y. Wang, and L. Chi, Langmuir. **25**, 3894 (2009).
13. L. Zhao, M. Vaupel, D. A. Loy, and K. J. Shea, Chem. Mater. **20**, 1870 (2008).

14. W. Shi, Y. Lin, S. He, Y. Zhao, C. Li, M. Wei, D. G. Evans, and X. Duan, J. Mater. Chem. **21**, 11116 (2011).
15. K. H. Chae, and Y. H. Kim, Adv. Func. Mater. **17**, 3470 (2007).
16. G. Pistolis, S. Boyatzis, M. Chatzichristidi, and P. Argitis, Chem. Mater. **14**, 790 (2002).
17. F. D. Benedetto, A. Biasco, R. Bizzarri, D. Arosio, F. Ricci, F. Beltram, R. Cingolani, and D. Pisignano, Langmuir. **22**, 29 (2006).
18. P. M. Bolger, W. Dickson, A. V. Krasavin, L. Liebscher, S. G. Hickey, D. V. Skryabin, and A. V. Zayats, Opt. Lett. **35**, 1197 (2010).
19. M. A. Noginov, G. Zhu, A. M. Belgrave, R. Bakker, V. M. Shalaev, E. E. Narimanov, S. Stout, E. Herz, T. Suteewong, and U. Wiesner, Nature, **460**, 1110 (2009).
20. S. V. Stoianov, C. Daengngam, M. Borhani, Y. Zhang, J. R. Morris, and H. D. Robinson, Appl. Mater. Interfaces. **4**, 2348 (2012).
21. W. Kern, and D. A. Poutinen, RCA Rev. **31**, 187 (1970).
22. J. Kerimo, D. M. Adams, and P. F. Barbara, J. Phys. Chem. B. **102**, 9451 (1998).
23. G. Schlegel, J. Bohnenberger, I. Potapova, and A. Mwes, Phys. Rev. Lett. **88**, 137401 (2002).
24. I. Ashry, B. Zhang, S. V. Stoianov, C. Daengngam, J. R. Heflin, H. D. Robinson, and Y. Xu, Opt. Lett. **37**, 1 (2012).

Chapter 7

Summary and Future Work

The following summarizes all of the results presented in this dissertation:

- LbL self-assembly technique can be used to control the distance between fluorophores and solid optical structures in nanometer accuracy. This can be achieved by changing the number of bilayers of the film.
- Fluorescence lifetime of fluorophores is dramatically modified by changing the thickness of a LbL film sandwiched between them and a plasmonic or semiconductor substrate.
- The intrinsic fluorescence lifetime and quantum yield of a fluorophore are independent of the environment surrounded to it.
- The modified PDOS near optical micro- and nano-structures can be experimentally probed after measuring the quantum yield, intrinsic lifetime, and modified lifetime of a fluorophore.
- Purcell effect can be utilized to measure the thickness of LbL films in nanoscale accuracy. The measurements obtained with this method agree well with those obtained with conventional thickness measurements tools such as, ellipsometry and AFM.
- LbL films assembled at pH > 8.5 are having pH-induced swelling/deswelling behavior. The hysteresis behavior during the swelling/deswelling cycle of a

LbL film that consists of PAH/PSS bilayers is larger than that of a one PAH monolayer.

- The pH-induced swelling/deswelling behavior of a LbL film of 5 PSS/PAH bilayers sandwiched between TR dyes and gold nanoparticles is used to modify the fluorescence dynamics of the dyes.
- UV laser directed through an evaporated aluminum mask ablates polymeric films to produce accurate micro-patterns with good fluorescent intensity when TR and QDs were used as fluorophores. This patterning process has no impact on the fluorescent dynamics of the used fluorophores.
- FIB has the ability to produce accurate nano-patterns with good fluorescent intensity, however, it affects the fluorescence dynamics of TR.
- Self-assembly of QDs over plasmonic nano-patterns does not affect the fluorescence lifetime of the QDs. The QDs assembled over the patterned region produce bright fluorescence compared with those assembled over flat substrate.

Future work

Based on the results obtained in this dissertation, we can suggest the following as a future work:

- Tunable metamaterials can be designed and fabricated using swellable LbL films. For example, PAH/PSS swellable LbL film can be incorporated within the metallic layers of the fishnet structure [1]. The LbL film thickness change during the swelling/deswelling cycles may modify the reflection and transmission spectra of the metamaterial structure. Furthermore, TR dyes can

be conjugated with the LbL film to investigate the effect of tuning the optical properties of metamaterials on the fluorescence dynamics of the dyes.

- Swellable LbL films can be used to design tunable Fano resonance optical structures. For instance, swellable LbL film incorporated within a double metallic grating can yield to Fano resonance in the visible range [2]. Therefore, if the LbL film contains fluorophores, the tuning of the Fano resonance wavelength may modify the fluorescence dynamics of them.
- LbL self-assembly can be used to incorporate fluorescent active gain media into plasmonic structures. This can help to compensate the strong dissipation in metallic systems which limits the range of plasmonic wave propagation and damps the strength of plasmonic resonance [3,4].
- TR dyes conjugated with swellable LbL film can be sandwiched between a flat plasmonic substrate and plasmonic nanoparticles. Changing the thickness of the film through the pH-induced swelling/deswelling may yield to strong modification in the fluorescence dynamics of the dyes.
- Fluorophores can be self-assembled above photonic crystals. The change of the fluorescence dynamics as a function of the distance between the fluorophores and the photonic crystals can be studied [5]. This study may be carried out when the emission wavelength of the fluorophores is within the bandgap of the photonic crystal or near its edge.

References

1. C. G. Meca, J. Hurtado, J. Marti, and A. Martinez, Phys. Rev. Lett. **106**, 067402 (2011).
2. B. Gallinet, and O. J. F. Martin, ACS Nano. **5**, 8999 (2011).
3. P. M. Bolger, W. Dickson, A. V. Krasavin, L. Liebscher, S. G. Hickey, D. V. Skryabin, and A. V. Zayats, Opt. Lett. **35**, 1197 (2010).
4. M. A. Noginov, G. Zhu, A. M. Belgrave, R. Bakker, V. M. Shalaev, E. E. Narimanov, S. Stout, E. Herz, T. Suteewong, and U. Wiesner, Nature, **460**, 1110 (2009).
5. A. F. Koenderink, M. Kafesaki, C. M. Soukoulis, and V. Sandoghdar, Opt. Lett. **30**, 3210 (2005).